



Energy harvesting using an inverted piezohydroelastic flag with resistor–inductor–capacitor circuit

Xiaobo Bi¹, Chenglei Wang¹, Qiang Zhu² and Hui Tang^{1,3,†}

¹Department of Mechanical Engineering, The Hong Kong Polytechnic University, Hung Hom, Kowloon, Hong Kong, PR China

²Department of Structural Engineering, University of California San Diego, La Jolla, California 92093-0085, USA

³The Hong Kong Polytechnic University Shenzhen Research Institute, Shenzhen, Guangdong 518057, PR China

(Received 8 June 2023; revised 22 August 2023; accepted 18 October 2023)

We develop a high-fidelity multi-physics model and, by using it, study the energy conversion process of a piezohydroelastic flag. Instead of a regular flag with a clamped upstream leading edge, we use an inverted flag so as to make the best of fluid elastic instability for energy harvesting. Moreover, different from many previous studies where a resistor–capacitor (RC) circuit is usually used, we adopt a resistor–inductor–capacitor (RLC) circuit for electricity generation. The influences of several key parameters associated with fluid, structure and electric dynamics are studied. Significantly different response modes are identified, among which the symmetric- and asymmetric-flutter modes are most suitable for sustainable energy harvesting, both emerging with moderate bending stiffness. If only deploying the RC circuit, increasing the resistance makes the flag more stable. By adding an inductor to turn the RC circuit into an RLC one, we observe the occurrence of ‘lock-in’ between the flag frequency and the circuit frequency as first reported on a regular flag by Xia *et al.* (*Phys. Rev. Appl.*, vol. 3, 2015, 014009). This phenomenon can significantly enhance the energy output, but it only happens when the circuit resistance is sufficiently large. From a derivation based on dynamic mode decomposition analysis, we further identify an optimal condition for maximizing the energy output, which can serve as a guideline to determine whether deploying an inductor can boost the performance, and, if yes, the required inductance. The findings from this study can better guide the design of flow-induced-vibration-based piezoelectric energy harvesters for microelectronic devices.

Key words: flow-structure interactions, wakes

† Email address for correspondence: h.tang@polyu.edu.hk

1. Introduction

Low-power electronics have been widely used in many areas such as implanted biomedical devices (Mitcheson *et al.* 2008; Paulo & Gaspar 2010) and wireless sensory nodes in remote or hostile locations for environmental monitoring (Shaikh & Zeadally 2016; Kanoun 2018). Conventionally, many of these electronics are powered by chemical batteries which necessitate periodic replacement and costly maintenance. To circumvent this situation, sustainable power generation can be achieved by extracting ambient energy. Some possible ambient energy sources are, for instance, thermal energy, light energy or flow energy. The present research focuses on the extraction of a ubiquitous source of flow energy via flow-induced vibration (FIV). Once triggered by fluid elastic instability, FIV is able to induce unsteady loads on structures. Classical FIV models include fluttering airfoils (Zhu & Peng 2009; Zhu 2011; Bibo & Daqaq 2013; Wang *et al.* 2020; Tamimi *et al.* 2022) and thin plates (Sodano, Inman & Park 2004; Dunnmon *et al.* 2011; Giacomello & Porfiri 2011; Xu-Xu, Barrero-Gil & Velazquez 2016; Qadri, Zhao & Tang 2020; Zhao *et al.* 2021) mounted in a uniform flow, cantilever beams placed in the Kármán vortex street behind a cylinder (Adhikari, Rastogi & Bhattacharya 2020; Du *et al.* 2022), galloping of bluff bodies (Barrero-Gil, Alonso & Sanz-Andres 2010; Tan, Zuo & Yan 2021), etc.

To convert the mechanical energy from ambient flows into electricity, there are several transduction mechanisms such as piezoelectric, electromagnetic and electrostatic generators, among which the piezoelectric transducer is of the major interest over the past decade due to its inherent electromechanical coupling and transduction capacity, ease of applications and high power density (Stojcev, Kosanovic & Golubovic 2009). Piezoelectricity refers to the phenomenon that piezoelectric material becomes polarized due to the accumulation of electric charge on the electrodes in response to applied mechanical stress (Cross 2004; Panda 2009). Through this mechanism, FIV-based piezoelectric transducers are able to provide stable power. As such, they have been considered as a promising alternative to batteries for low-power electronics (Uchino 2018; Hamlehdar, Kasaeian & Safaei 2019; Safaei, Sodano & Anton 2019).

Many experimental, theoretical and numerical efforts have been spent to explore the energy conversion process of FIV-based piezoelectric transducers, on which Hamlehdar *et al.* (2019) have done a comprehensive review. Experimental studies (e.g. Dunnmon *et al.* 2011; Hobbs & Hu 2012; Song *et al.* 2015; Petrini & Gkoumas 2018) have demonstrated the feasibility and reliability of the FIV-based piezoelectric transducer under various conditions. Theoretical studies, such as those conducted by Abdelkefi, Nayfeh & Hajj (2012) and Tan, Yan & Hajj (2016), used decoupled electromechanical models to analyse the dynamics of FIV-based piezoaeroelastic systems. However, these decoupled models oversimplified the sophisticated fluid–structure interactions. To address this issue, a number of coupled fluid–structure–electric models have been developed in the past decade. For example, Doaré & Michelin (2011) and Michelin & Doaré (2013) developed such a multi-physics model to study a two-dimensional elastic plate placed in an axial flow. The plate experiences self-sustained flutter when the flow velocity exceeds a critical value (Connell & Yue 2007; Alben & Shelley 2008). Electricity is then generated via distributed piezoelectric patches that are applied along the plate's surface. They found that energy harvesting efficiency of this system is optimized when the flutter frequency is tuned to the time scale of the electric system. De Marqui, Erturk & Inman (2010) presented a piezoaeroelastic model combining an unsteady vortex-lattice model and an electromechanically coupled finite-element model to investigate the electrical power output of a cantilever plate placed on the flexible wing of micro air vehicles.

Although revealing useful physical insights in the energy conversion mechanism, the above coupled fluid–structure–electric models employed either the slender body theory or the potential flow theory to describe the fluid dynamics, which may not be applicable to low- or intermediate-Reynolds-number flows in which most low-power electromechanical devices are operated (Taylor *et al.* 2001; Wang & Ko 2010; Wang & Liu 2011). To address this issue, Akcabay & Young (2012) and Shoele & Mittal (2016) developed new sets of fully coupled fluid–structure–electric models, in which the fluid dynamics is described by the Navier–Stokes equations and the interactions between the viscous flow and the piezoelectric structure are dealt with by the immersed boundary method (Peskin 2002). In these studies, the impacts of many parameters such as density ratio, Reynolds number, electromechanical coupling coefficient, etc. upon the piezohydroelastic system have been extensively investigated. The difference of these two studies lies in the piezoelectric patch configuration: the former utilized the single-patch configuration while the latter used distributed piezoelectric patches.

Existing studies have also revealed some scenarios where the energy harvesting performance of FIV-based piezoelectric transducers can be enhanced. Such improvements can be achieved through manipulations in fluid, structure or electrical domains, either separately or collectively. For example, from the fluid perspective, Mazharmanesh *et al.* (2022) found that, compared with in uniform flows, a piezoelectric flag placed in oscillating flows is able to create much higher energy due to constructive interactions between the vorticity flow and the flag. From the structure perspective, inverted flags, clamped at the downstream trailing edge and free to flap at the upstream leading edge, are found to be beneficial to energy harvesting (Kim *et al.* 2013; Ryu *et al.* 2015; Tang, Liu & Lu 2015). Compared with regular flags with clamped upstream leading edge, inverted flags are far more unstable and are able to produce sustained large-amplitude vibrations in a wider range of bending rigidity and flow speeds (Shoele & Mittal 2016).

As for the electrical circuit, most existing studies only considered the simplest resistor–capacitor (RC) circuit, i.e. a capacitor rendered by the piezoelectric material's intrinsic feature and a resistor representing the electrical load (Doaré & Michelin 2011; Michelin & Doaré 2013; Dias, De Marqui & Erturk 2014; Shoele & Mittal 2016; Safaei *et al.* 2019; Mazharmanesh *et al.* 2022). Energy harvesting performance can be enhanced by introducing an inductor into this conventional RC circuit, forming a resistor–inductor–capacitor (RLC) circuit that intrinsically has a resonant frequency. By inheriting the fully coupled model used in Michelin & Doaré (2013) and deploying an RLC circuit on a regular flag, Xia, Michelin & Doaré (2015) found that the flapping frequency of the flag was locked onto the circuit's natural frequency under certain circumstances, leading to a wider operating frequency bandwidth and an enhanced efficiency. A similar observation was also made by Wang *et al.* (2016). Moreover, by applying a decoupled model to a regular flag, Tan & Yan (2017) concluded that simultaneous tuning of the resistance and the inductance can achieve better energy harvesting efficiencies than tuning the resistance alone.

Clearly, the existing studies have suggested that inverted flags can generally perform better than regular flags in terms of energy generation, and RLC-circuit-based flags may perform better than RC-circuit-based flags. Intuitively, one would expect that RLC-circuit-based inverted flags can exhibit the best performance. However, so far, no study has been reported on such a highly promising configuration. To this end, the current study aims at developing a fully coupled fluid–structure–electric model and using it to study the energy conversion of an inverted piezohydroelastic flag mounted in a viscous flow. The fluid dynamics will be depicted with the Navier–Stokes equations and the

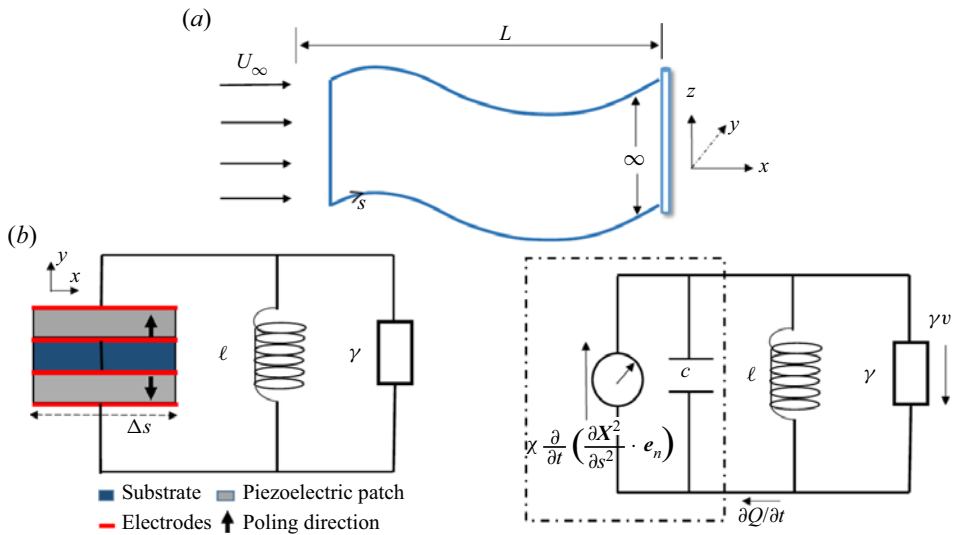


Figure 1. (a) Schematic of the inverted piezoelectric flag. (b) Electric circuit of a piezoelectrical patch pair connected with the output loop and the equivalent RLC circuit.

fluid–structure coupling will be handled by the immersed boundary method. An RLC circuit will be applied for the electricity generation. With this multi-physics model, we explore the characteristics of the inverted piezohydroelastic flag system, particularly the influence of the RLC circuit on the dynamics of the flag and the resulting energy harvesting performance.

2. Physical problem

As shown in [figure 1\(a\)](#), the inverted flag we consider here is reduced to a cantilevered plate with length L and infinite span, subjected to a parallel fluid flow of speed U_∞ moving from the free leading edge to the clamped trailing edge. The plate is assumed to be thin and inextensible, and only its out-of-plane deformation is considered. As such, we can use a two-dimensional Euler–Bernoulli beam model to describe its structural dynamics.

The lower and upper surfaces of the flag are covered by piezoelectric layers (referred to as the bimorph configuration (Bonello & Rafique 2011); see [figure 1\(b\)](#)), which contain continuous piezoelectrical patch pairs of infinitesimal length (Bisegna, Caruso & Maceri 2006; Doaré & Michelin 2011). The patch pairs are connected in series with opposite polarity. The electrodes are coupled with the power output circuit consisting of a resistor and an inductor, which are connected in parallel. As the piezoelectric material is deformed by the local curvature of the flag, the electrodes will have a potential difference so that an electric current can be generated in the circuit. The power dissipated by the resistor as the electric current passes through is the harvested energy.

3. Problem formulations

3.1. Governing equations for the coupled fluid–structure–electric system

Described in the Eulerian coordinate $x \equiv (x, y)$, the fluid dynamics is governed by the incompressible Navier–Stokes (N–S) equations with constant fluid density ρ and

viscosity μ . The dimensionless N–S equations are

$$\left. \begin{aligned} \frac{\partial \mathbf{u}}{\partial t} + \nabla \cdot (\mathbf{u}\mathbf{u}) &= -\nabla p + \frac{1}{Re} \nabla^2 \mathbf{u} + \mathbf{f}(\mathbf{x}) \quad \text{and} \\ \nabla \cdot \mathbf{u} &= 0, \end{aligned} \right\} \quad (3.1)$$

in which \mathbf{u} represents the fluid velocity vector, p the pressure, $Re \equiv \rho U_\infty L / \mu$ the Reynolds number and \mathbf{f} the fluid–structure interaction force density.

The three-layer ‘sandwich’ in figure 1 is modelled as an Euler–Bernoulli beam. Let $\mathbf{X}(s, t)$ denote the instantaneous displacement vector of an arbitrary structural element at the Lagrangian location s , the conservation of momentum and the inextensibility constraint (i.e. $\partial \mathbf{X} / \partial s \cdot \partial \mathbf{X} / \partial s = 1$) for the flag lead to

$$\left. \begin{aligned} m_s \frac{\partial^2 \mathbf{X}(s, t)}{\partial t^2} &= \frac{\partial}{\partial s} \left[\sigma(s, t) \mathbf{e}_\tau - \frac{\partial M(s, t)}{\partial s} \mathbf{e}_n \right] - \mathbf{F}(s, t) + m_s \mathbf{g}, \\ \mathbf{X} &= \mathbf{X}_0 \quad \text{and} \quad \frac{\partial \mathbf{X}}{\partial s} = (1, 0), \quad \text{at the trailing edge} \\ M &= 0 \quad \text{and} \quad \sigma \mathbf{e}_\tau - \frac{\partial M}{\partial s} \mathbf{e}_n = 0, \quad \text{at the leading edge} \end{aligned} \right\} \quad (3.2)$$

where m_s is the mass per unit length of the beam and \mathbf{F} stands for the hydrodynamic loading. The gravity acceleration \mathbf{g} is set as zero throughout the manuscript unless otherwise stated (it is only involved in Appendix A.1). Here, \mathbf{e}_n and \mathbf{e}_τ are, respectively, the unit normal and tangential vectors, defined as $\mathbf{e}_\tau = \partial \mathbf{X} / \partial s$ and $\mathbf{e}_n = (0, 0, 1) \times \mathbf{e}_\tau$ and \mathbf{X}_0 is the initial position of the flag. The tension force σ is determined by the constraint of inextensibility (Huang, Shin & Sung 2007)

$$\frac{\partial^2}{\partial s^2} (\sigma \mathbf{e}_\tau) \cdot \mathbf{e}_\tau = \frac{m_s}{2} \frac{\partial^2}{\partial t^2} (\mathbf{e}_\tau \cdot \mathbf{e}_\tau) - m_s \frac{\partial \mathbf{e}_\tau}{\partial t} \cdot \frac{\partial \mathbf{e}_\tau}{\partial t} + \frac{\partial}{\partial s} \left[\frac{\partial}{\partial s} \left(\frac{\partial M}{\partial s} \mathbf{e}_n \right) + \mathbf{F} - m_s \mathbf{g} \right] \cdot \mathbf{e}_\tau. \quad (3.3)$$

In (3.2), M is the total internal bending moment of the piezoelectric flag resulting from the flag’s deformation and the reverse piezoelectric effect of the piezoelectric patches, i.e.

$$M = k_b \frac{\partial^2 \mathbf{X}}{\partial s^2} \cdot \mathbf{e}_n - \chi v(s, t), \quad (3.4)$$

in which k_b is the bending stiffness, χ the structure–electric coupling coefficient and v the electric voltage. We consider a continuous distribution of patches (Doaré & Michelin 2011; Michelin & Doaré 2013) such that the voltage v and electrical charge displacement Q are continuous functions of the flag’s location s . Based on Gauss’ law (Jackson & David 1998), the electrical equation for the RLC circuit is

$$\left. \begin{aligned} \frac{\partial Q}{\partial t} + \gamma v + \int_0^t \frac{v(\tau)}{\ell} d\tau &= 0, \\ Q &= cv + \chi \frac{\partial^2 \mathbf{X}}{\partial s^2} \cdot \mathbf{e}_n. \end{aligned} \right\} \quad (3.5)$$

It can be further reduced to

$$c \frac{\partial^2 v}{\partial t^2} + \gamma \frac{\partial v}{\partial t} + \frac{v}{\ell} = -\chi \frac{\partial^2}{\partial t^2} \left(\frac{\partial^2 \mathbf{X}}{\partial s^2} \cdot \mathbf{e}_n \right), \quad (3.6)$$

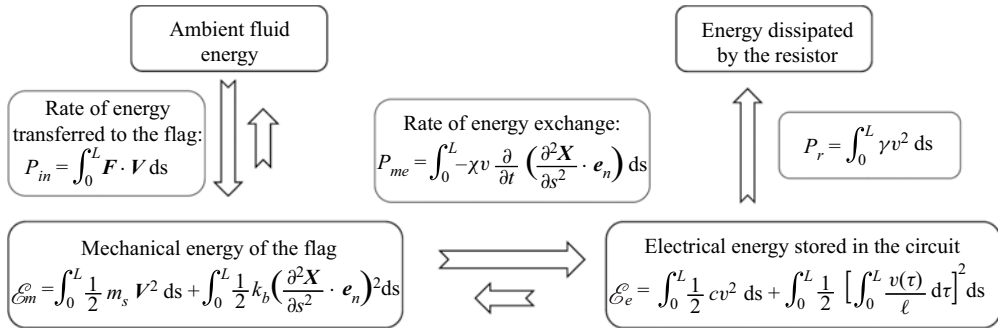


Figure 2. The energy transfer pathway of a piezohydroelastic flag.

where c is the intrinsic capacitance of the piezoelectric patch pair, γ the lineic conductivity of the resistor (inverse of the resistance R) and ℓ the inductance.

The coupling of the fluid and piezoelastic dynamics is accomplished with the immersed boundary method (IBM). The IBM-based fluid–structure interaction algorithm has been well documented in past studies (Peskin 2002; Bi & Zhu 2019), herein, we only briefly sketch its key points. The fluid–structure interacting forces $\mathbf{f}(\mathbf{x}, t)$ and $\mathbf{F}(s, t)$ are defined in the Eulerian and Lagrangian coordinates, respectively. The transformation between these two quantities is achieved by using the Dirac delta function

$$\mathbf{f}(\mathbf{x}, t) = \int_{\Gamma} \mathbf{F}(s, t) \delta(\mathbf{x} - \mathbf{X}(s, t)) \, ds, \quad (3.7)$$

in which Γ represents the Lagrangian domain. Following Goldstein, Handler & Sirovich (1993), \mathbf{F} is calculated by

$$\mathbf{F}(s, t) = \tilde{\alpha} \int_0^t [\mathbf{U}(s, \tau) - \mathbf{V}(s, \tau)] \, d\tau + \tilde{\beta} [\mathbf{U}(s, t) - \mathbf{V}(s, t)], \quad (3.8)$$

where $\tilde{\alpha}$ and $\tilde{\beta}$ are sufficiently large negative constants (Goldstein *et al.* 1993), $\mathbf{V}(s, t)$ is the structural velocity, i.e. $\mathbf{V} = \partial \mathbf{X} / \partial t$, $\mathbf{U}(s, t)$ denotes the local fluid velocity at the immersed structural position s , which is calculated by

$$\mathbf{U}(s, t) = \int_{\Omega} \mathbf{u}(\mathbf{x}, t) \delta(\mathbf{x} - \mathbf{X}(s, t)) \, d\mathbf{x}, \quad (3.9)$$

where Ω denotes the fluid domain. Since the fluid and structure dynamics are solved independently, the matching of \mathbf{U} and \mathbf{V} is achieved by (3.8), through which a penalty force will be generated, which converges to the physical fluid–structure interaction force after iterations.

The energy transfer pathway of the piezohydroelastic system is presented in figure 2. The ambient flow powers the flag at a rate of P_{in} , leading to substantial mechanical energy \mathcal{E}_m (including the kinetic energy and the strain energy) being stored in the flag. A portion of \mathcal{E}_m is converted to electric energy \mathcal{E}_e at a rate of P_{me} , which is stored in the piezoelectric capacitor and the inductor in the output electric circuit. The electricity will then be dissipated by the resistor at a rate of P_r ; P_r is always positive according to its nature, but the instantaneous values of the other two energy transfer rates P_{in} and P_{me} can be negative during certain time intervals. For this reason, reversed arrows are added beside the main arrows. Nevertheless, the energy is mainly transferred along the main arrows and

the time-averaged values of these two energy transfer rates are positive. According to the law of energy conservation, we have

$$\frac{d\mathcal{E}_m}{dt} = P_{in} - P_{me}, \quad \frac{d\mathcal{E}_e}{dt} = P_{me} - P_r. \quad (3.10a,b)$$

When the system achieves its periodic steady state, we have $\langle P_r \rangle = \langle P_{me} \rangle = \langle P_{in} \rangle$, where $\langle \cdot \rangle$ denotes the time-averaging operator.

The performance of the system is evaluated through energy harvesting efficiency C_p , the ratio between the time-averaged power expenditure by the resistor and the theoretical upper limit of the flow-energy flux past the projected area that is swept by the fluttering flag, i.e.

$$C_p = \frac{\langle P_r \rangle}{\frac{1}{2}\rho 2LU_\infty U_\infty^2} = \frac{\langle P_r \rangle}{\rho LU_\infty^3}. \quad (3.11)$$

In the present work, the characteristic length, velocity, density and voltage are chosen as L , U_∞ , ρ and $U_\infty\sqrt{\rho L/c}$, respectively. The electroelastic equations ((3.2) and (3.6)) can be non-dimensionalized as

$$\left. \begin{aligned} \frac{1}{m^*} \frac{\partial^2 \mathbf{X}}{\partial t^2} &= \frac{\partial}{\partial s} (\sigma(s, t) \mathbf{e}_\tau) - \frac{\partial}{\partial s} \left[K^* \frac{\partial^3 \mathbf{X}}{\partial s^3} - \alpha \sqrt{K^*} \frac{\partial v}{\partial s} \mathbf{e}_n \right] - \mathbf{F}(s, t), \\ \frac{\partial^2 v}{\partial t^2} + \frac{1}{\beta} \frac{\partial v}{\partial t} + \omega_0^2 v &= -\alpha \sqrt{K^*} \frac{\partial^2}{\partial t^2} \left(\frac{\partial^2 \mathbf{X}}{\partial s^2} \cdot \mathbf{e}_n \right), \end{aligned} \right\} \quad (3.12)$$

in which m^* represents the inertial ratio between the fluid and structure, K^* the normalized bending stiffness, α the normalized electromechanical coupling coefficient, β the normalized resistance and ω_0 the natural frequency of the electrical circuit, defined as follows:

$$m^* = \frac{\rho L}{m_s}, \quad K^* = \frac{k_b}{\rho U_\infty^2 L^3}, \quad \alpha = \frac{\chi}{\sqrt{k_b c}}, \quad \beta = \frac{c U_\infty}{\gamma L}, \quad \omega_0 = \frac{L}{U_\infty \sqrt{\ell c}}. \quad (3.13a-e)$$

Note that Michelin & Doaré (2013) and Shoele & Mittal (2016) used $1/U^*{}^2$ to replace K^* , where U^* is defined as the normalized free-stream velocity. In addition, the power harvesting efficiency C_p can also be viewed as the non-dimensional time-averaged energy harvested by the system:

$$C_p = \left\langle \int_0^1 v^2 ds \right\rangle / \beta. \quad (3.14)$$

Hereafter, all simulation results will be presented in the non-dimensional form.

3.2. Numerical implementation

The hydrodynamic equations (3.1) are spatially discretized using the finite difference approach over a set of staggered Cartesian grids. The Crank–Nicolson scheme is used to temporally discretize the diffusion and convection terms. The discrete form of the

equations becomes

$$\left. \begin{aligned} \frac{\mathbf{u}^{n+1} - \mathbf{u}^n}{\Delta t} + \frac{\mathcal{H}(\mathbf{u}^{n+1}) + \mathcal{H}(\mathbf{u}^n)}{2} &= -\mathcal{G}(p^{n+1/2}) + \frac{\mathcal{L}(\mathbf{u}^{n+1}) + \mathcal{L}(\mathbf{u}^n)}{2Re} + \mathbf{f}^{n+1}, \\ \mathcal{D}(\mathbf{u}^{n+1}) &= 0, \end{aligned} \right\} \quad (3.15)$$

where Δt is the time step, the superscript ‘ $n + 1$ ’ denotes the $(n + 1)$ th time step. Here, \mathcal{H} represents the discrete convective operator, \mathcal{L} the discrete Laplace operator, \mathcal{G} the discrete gradient operator and \mathcal{D} the discrete divergence operator. Following Kim, Baek & Sung (2002), the discrete hydrodynamic equations are solved with a projection method. The general process of updating the flow velocity and pressure fields is well documented in this reference.

Regarding the numerical treatment for the piezoelectric equations, uniform staggered grids are also used to discretize the body along s . A fully implicit time advancement method is employed, leading to the discrete piezoelectric equations

$$\begin{aligned} \frac{1}{m^*} \frac{X^{n+1} - 2X^n + X^{n-1}}{\Delta t^2} &= D_s(\sigma^{n+1/2} D_s X^{n+1}) - K^* D_{ssss} X^{n+1} \\ &+ \alpha \sqrt{K^*} D_s (D_s v^{n+1} \mathbf{e}_n^{n+1}) - \mathbf{F}^{n+1}, \end{aligned} \quad (3.16)$$

and

$$\begin{aligned} \frac{v^{n+1} - 2v^n + v^{n-1}}{\Delta t^2} + \frac{v^{n+1} - v^n}{\beta \Delta t} + \omega_0^2 v^{n+1} \\ = \alpha \sqrt{K^*} \frac{D_{ss} X^{n+1} \cdot \mathbf{e}_n^{n+1} - 2D_{ss} X^n \cdot \mathbf{e}_n^n + D_{ss} X^{n-1} \cdot \mathbf{e}_n^{n-1}}{-\Delta t^2}, \end{aligned} \quad (3.17)$$

where D_s , D_{ss} and D_{ssss} are the first-, second- and fourth-order central difference operators with respect to s , respectively. The tension $\gamma^{n+1/2}$ is calculated by

$$\begin{aligned} D_{ss}(\sigma^{n+1/2} \mathbf{e}'_\tau) \cdot \mathbf{e}'_\tau &= \frac{1 - 2(\mathbf{e}_\tau \cdot \mathbf{e}_\tau)^n + (\mathbf{e}_\tau \cdot \mathbf{e}_\tau)^{n-1}}{2m^* \Delta t^2} - \frac{1}{m^*} (D_s V' \cdot D_s V') \\ &+ D_s \left[K^* D_{ssss} X' - \alpha \sqrt{K^*} D_s (D_s v' \mathbf{e}_n^n) + \mathbf{F}' \right] \cdot \mathbf{e}'_\tau, \end{aligned} \quad (3.18)$$

in which the superscript prime represents the intermediate time step, indicating the variables will be updated during feedback iterations.

The following time-marching method including two feedback loops is chosen to resolve the coupled hydrodynamic and piezoelectric equations:

- (i) Solve (3.15) for \mathbf{u}^{n+1} .
- (ii) Update the penalty force \mathbf{F} via (3.8) and (3.9) by using the updated \mathbf{u}^{n+1} .
- (iii) Solve (3.16) and (3.18) for X^{n+1} , then update \mathbf{F} through (3.8)–(3.9).
- (iv) Update v^{n+1} via (3.17).
- (v) Repeat steps (iii) to (iv) until the convergence of the piezoelectric solutions.
- (vi) Update \mathbf{f} by using (3.7).
- (vii) Repeat steps (i) to (vi) until the fluid field \mathbf{u}^{n+1} converges.

More details of this numerical scheme can be found in Shoele & Mittal (2016).

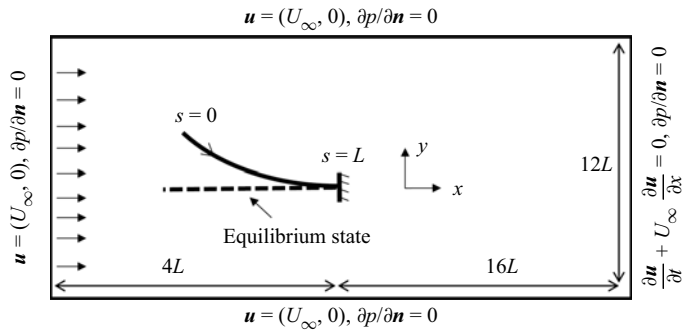


Figure 3. Computational domain (not to scale) and boundary conditions.

All simulations will be performed in the rectangular domain depicted in [figure 3](#), where the boundary conditions are also specified. There are 500×400 grid nodes in the x and y directions. A uniform grid size $\Delta x = \Delta y = 0.011$ is used in the vicinity of the flag, whose structural grid size is chosen to be $\Delta s = 0.0067$. A constant time step $\Delta t = 0.0002$ is employed. All these numerical parameters are determined based on a series of sensitivity tests.

The accuracy of our fluid–structure–electrical numerical model is confirmed multi-hierarchically through comparisons with benchmark results (see [Appendix A](#)).

4. Results and discussion

We conduct multi-physics simulations using the above coupled structure–fluid–electrical model to study the energy harvesting performance of the inverted piezohydroelastic flag. The dynamics of the system is dependent upon the five non-dimensional parameters listed in [\(3.13a–e\)](#) plus the Reynolds number Re . As revealed in [Shoole & Mittal \(2016\)](#), the dynamics of the piezoelectric flag is very similar when Re lies in the range of 25–800. Hence, in the present study Re is fixed at 200, which is sufficiently high to capture the key features of the system and, in the meantime, not computationally expensive. Although the density ratio, m^* , is also a key factor determining the dynamics and energy harvesting performance of the system, its influence has been extensively studied in literature and hence is fixed at $m^* = 1.0$ in the present study. The electromechanical coupling coefficient, α , describes the coupling strength between the mechanical part and the output circuit. In this study, we only focus on the strong coupling scenario in favour of high energy conversion rate, and choose a high value, i.e. $\alpha = 0.9$, unless otherwise mentioned. As such, we will concentrate on the influences of the remaining three parameters, i.e. K^* , β and ω_0 , respectively characterizing the structural bending stiffness, resistive and inductive properties of the electrical circuit, on the dynamics and energy harvesting performance of the system.

4.1. Structural response

In what follows, we explore the structural dynamics of the inverted piezohydroelastic flag with three representative bending rigidity values $K^* = 0.1, 0.25, 0.4$ (0.1 represents a super flexible flag while 0.4 connotes a very stiff one), in a large electrical parameter space, i.e. $10^{-2} \leq \beta \leq 10^2$ and $0 \leq \omega_0 \leq 10$. Since our simulations show that the flag tends to stay undeformed (referred to as the ‘straight mode’) ([Kim *et al.* 2013](#)) as the

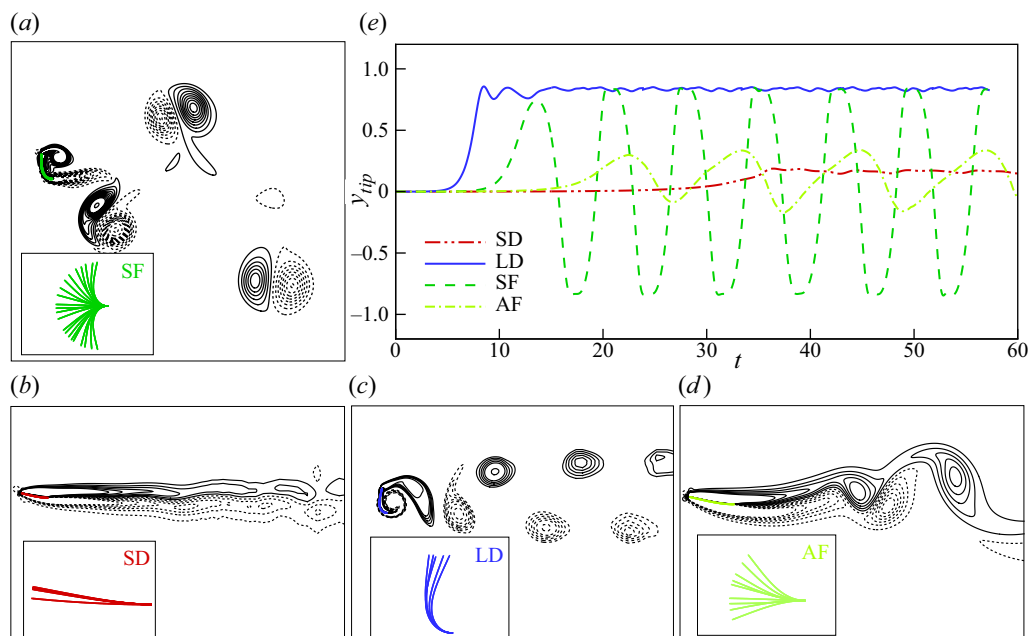


Figure 4. (*a–d*) Deformation and wake patterns of various dynamic modes: (*a*) the symmetric-flutter (SF) mode, (*b*) the small-deflection (SD) mode, (*c*) the large-deflection (LD) mode, (*d*) the asymmetric-flutter (AF) mode. The contours are based on vorticity (dashed contours represent counterclockwise vortices with negative vorticity). The insets present the corresponding full body profiles. (*e*) Time histories of the vertical displacement of the flag tip in different dynamic modes. Panels show (*a*) $K^* = 0.25$, $\beta = 0.1$, $\omega_0 = 10$; (*b*) $K^* = 0.4$, $\beta = 1.0$, $\omega_0 = 0.5$; (*c*) $K^* = 0.1$, $\beta = 10$, $\omega_0 = 5.0$; (*d*) $K^* = 0.25$, $\beta = 10$, $\omega_0 = 0$.

bending rigidity reaches the level of $K^* = 0.5$, this scenario will be excluded from our consideration.

Four dynamic modes are observed, namely the symmetric-flutter mode where the flag performs symmetric-flutter motion about its equilibrium position, the small-deflection mode where the flag slightly deforms to one side, the large-deflection mode where the flag significantly deforms to one side and the asymmetric-flutter mode where the flag performs flutter motion but the upward and downward strokes are asymmetric about its equilibrium position. Figure 4 presents the time histories of the lateral displacement of the flag free tip, y_{tip} , and the body profiles of these four dynamic modes. These modes are consistent with those observed in previous studies (Kim *et al.* 2013; Cerdeira *et al.* 2021), in which the dynamics of inverted flags (without electric circuits) was experimentally investigated for various bending rigidity values and mass ratios, indicating that the inclusion of electric circuits does not induce any new response mode. Only when the two flutter modes are exhibited, i.e. the symmetric- and asymmetric-flutter modes, does the flag undergo large-amplitude oscillations so that it can continuously and effectively extract flow energy.

Figure 4 also presents the wake patterns of these dynamic modes. As shown in figure 4(*b*), the wake of the small-deflection mode is characterized by a pair of shear layers, developed from both the upper and lower surfaces of the flag, which are elongated and eventually break up due to the Kelvin–Helmholtz instability. In the large-deflection mode, the large mean deformation and small-amplitude oscillation make the flag behave like a bluff body. As a result, vortices of opposite signs alternatively shed from the leading and trailing edges of the flag, leading to a typical Kármán vortex street in the wake

Energy harvesting using an inverted flag with RLC circuit

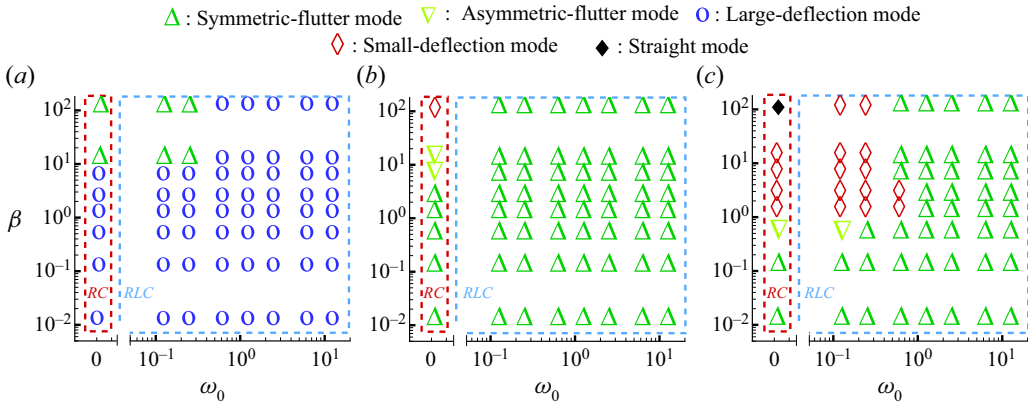


Figure 5. Distribution of dynamic modes in the $\beta - \omega_0$ space for flags of different bending stiffness. Panels show (a) $K^* = 0.1$, (b) $K^* = 0.25$, (c) $K^* = 0.4$.

(i.e. the S mode) as shown in [figure 4\(c\)](#). In the symmetric-flutter mode shown in [figure 4\(a\)](#), a pair of opposite-signed vortices shed from the leading edge once the flag reaches either one of its stroke extremes, which then propagate downstream with a prominent angle. As a result, two streets of vortex pairs (i.e. the 2P mode) appear in the wake. Differently, in the asymmetric-flutter mode the flag flutters with a much smaller amplitude and a lower frequency, as can be read in [figure 4\(e\)](#). As such, only one pair of vortices are generated during one flapping period, forming a 2S-mode vortex street with very small lateral distance, as shown in [figure 4\(d\)](#).

[Figure 5](#) maps the structural dynamics of the inverted piezohydroelastic flag in the electrical parameter space. Here, we use green markers (both up-pointing and down-pointing triangles) to denote the symmetric- and asymmetric-flutter modes that are appropriate for flow-energy harvesting. When the flag is super flexible with $K^* = 0.1$, there is only a small green region in the upper left corner of [figure 5\(a\)](#), while all the remaining cases belong to the unsuitable large-deflection mode. This is not surprising because a too soft flag fails to provide sufficient recovery bending moment for sustainable flutter motion. On the other hand, as the flag becomes very stiff with $K^* = 0.4$ ([figure 5c](#)), the cases in the upper left corner are in the small-deflection mode or even remain undeformed (i.e. in the straight mode), and hence inappropriate for flow-energy harvesting. Only when the flag is moderately flexible with $K^* = 0.25$ does the system undergo the symmetric- or asymmetric-flutter motions in most of the map except for the case with the small-deflection mode at $\beta = 10^2$ and $\omega_0 = 0$ (see [figure 5b](#)).

Note that all the cases in the first column of each panel of [figure 5](#) are only equipped with an RC circuit, where $\omega_0 = 0$. Furthermore, with the smallest resistance (i.e. $\beta = 10^{-2}$) the bottom left case approximates the short-circuit case (or, equivalently, the case without piezoelectric effect, i.e. $\alpha = 0$), whereas with the largest resistance (i.e. $\beta = 10^2$), the upper left case approximates the open-circuit case. From the results in this column, it is interesting to see that increasing the resistance in the output RC circuit makes the flag appear stiffer, or in other words, more stable. Specifically, as β increases, the flag changes from the large-deflection mode to the symmetric-flutter mode in [figure 5\(a\)](#), from the symmetric-flutter mode to the asymmetric-flutter mode and then to the small-deflection mode in [figure 5\(b\)](#) and from the symmetric-flutter mode all the way to the straight mode in [figure 5\(c\)](#).

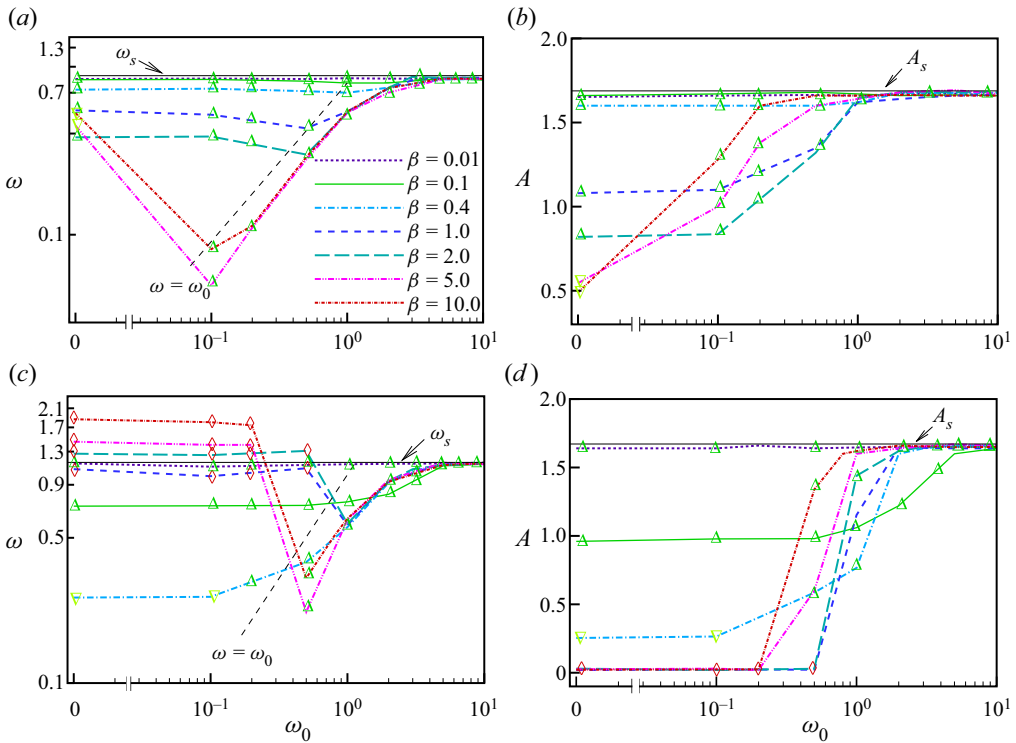


Figure 6. Variations of flapping frequency (a,c) and amplitude (b,d) against ω_0 for the moderate flexible flag ((a,b), $K^* = 0.25$) and the less flexible flag ((c,d), $K^* = 0.4$) equipped with various resistances β in the electrical circuit. Here, ω_s and A_s , indicated by black solid lines, are the flapping frequency and amplitude of the flag with no electromechanical coupling, respectively.

Figure 6 further shows the variations of the flag’s dominant flapping frequency ω and amplitude A against the electrical circuit’s undamped natural frequency ω_0 at selected resistance and bending stiffness values. Here, ω is calculated by Fourier analysis of the time histories of vertical displacement of the flag tip, y_{tip} , and A is obtained by measuring the difference between the upper and lower bounds of y_{tip} . Since in the present study the flag neither experiences high-order oscillations nor reverses its leading-edge tip, A is positively correlated with its maximum curvature. Mode types identified in figure 5 are also marked in the figure with the same set of symbols. As baseline values, the frequency and amplitude of the flag with no electromechanical coupling (i.e. $\alpha = 0$), referred to as ω_s and A_s , respectively, are also presented as black solid straight lines.

When the resistance is trivial (e.g. $\beta = 0.01$), the flapping frequency and amplitude are very close to the baseline values, because under this condition the RLC circuit is almost short circuited by the resistor. As a result, the circuit has almost no influence on the flag deformation, which is reminiscent of the electroelastic coupling coefficient α being zero. Similarly, when ω_0 is sufficiently large (equivalently when the lineic admittance $1/\ell$ of the inductor is sufficiently small according to (3.13a–e)), the RLC circuit is then short circuited by the inductor. Consequently, the structural responses with respect to both the flapping frequency and amplitude converge to the baseline values asymptotically regardless of the β value.

Only when β is not too small and ω_0 is not too large does the electrical circuit exert a significant impact on the structural dynamics. It shows that varying ω_0 may lead

to mode transition. For example, in [figure 6\(a\)](#) the asymmetric-flutter mode (∇ , lime) appearing in the RC circuit is transitioned into the symmetric-flutter mode (Δ , green) after implementing a small inductor ($\omega_0 = 0.1$) into the circuit. The mode transition in [figure 6\(c\)](#), however, takes place in the RLC circuit, where the most noticeable one is between the small-deflection mode (\diamond , red) and the symmetric-flutter mode (Δ , green).

These mode transitions are usually accompanied by an abrupt change in the flag's dominant flapping frequency ω and amplitude A . In particular, as shown in [figure 6\(a,c\)](#), ω plunges during the transition, followed by a continuous rise up to ω_s with a slope close to that of the line $\omega = \omega_0$, suggesting a 'lock-in' phenomenon. As revealed in the following sections, in this 'lock-in' regime, the flag will resonate with the circuit, leading to an enhanced energy output. A similar observation has been made by Wang *et al.* (2016) when examining a regular piezoelectric flag, who also revealed that during this 'lock-in' the flag is able to flutter at much lower speeds. Note that, in both studies, ω is consistently smaller than ω_0 , the undamped natural frequency of the circuit, in the 'lock-in' regime, different from what was reported in Xia *et al.* (2015), where the two frequencies coincide with each other. This frequency reduction reflects the damped and nonlinear nature of the current coupled fluid–structure–electrical system. This 'lock-in' becomes less pronounced as β decreases towards the short-circuit scenario. As shown in [figure 6\(a,c\)](#), the 'lock-in' phenomenon even vanishes when $\beta \leq 0.4$ for the moderate flexible flag (i.e. $K^* = 0.25$) and $\beta \leq 0.1$ for the less flexible flag (i.e. $K^* = 0.4$).

4.2. Energy harvesting performance

The electrical parameters β and ω_0 characterize the resistive and inductive properties of the circuit, respectively, affecting the energy extraction performance of the inverted piezohydroelastic flag. In this section, we explore how they influence the energy output of the flag and pin down the underlying physics.

4.2.1. The RC circuit

The impact of β on the energy output in the scenario of the RC circuit (i.e. $\omega_0 = 0$) is presented in [figure 7](#). Since the stiff flag (i.e. $K^* = 0.4$) displays multiple modes in this scenario, here, we only consider the moderate flexible flag (i.e. $K^* = 0.25$) for simplicity. It is not surprising to see that trivial energy is harvested when β is too small ($\beta \ll 1$) or too large ($\beta \gg 1$), corresponding to the short- and open-circuit conditions, respectively. A peak energy output is then achieved at a moderate β value between 0.1 and 1. Similar observations have also been reported in Michelin & Doaré (2013) and Shoele & Mittal (2016). They attributed the optimal performance to the 'resonance' achieved by matching the electrical time scale and the mechanical time scale, i.e. $\omega\beta \sim O(1)$. In the present study, the energy peak appears at approximately $\omega\beta = 0.22$, as denoted in [figure 7](#), confirming the above statement on optimal condition but near the lower bound of $O(1)$. Our discussions in the following part and the result presented in [figure 16](#) of [Appendix A.3](#) further suggest that this near-the-lower-bound optimal condition can be attributed to the enhanced damping due to the much stronger electromechanical coupling $\alpha = 0.9$ applied here (instead of $\alpha = 0.5$ in Michelin & Doaré 2013; Shoele & Mittal 2016).

In what follows, we attempt to elaborate on the energy transfer mechanism through mode analysis. As described in (3.12), the circuit undergoes damped oscillations forced by an excitation term originated from the curvature of the flag, i.e. $\Lambda(s, t) = (\partial^2 X / \partial s^2) \cdot \mathbf{e}_n$. A dynamic-mode-decomposition (DMD) analysis (Kutz *et al.* 2016) is then conducted on a time series of snapshots of Λ with an equal time interval $\Delta T = 0.0125$. The electrical

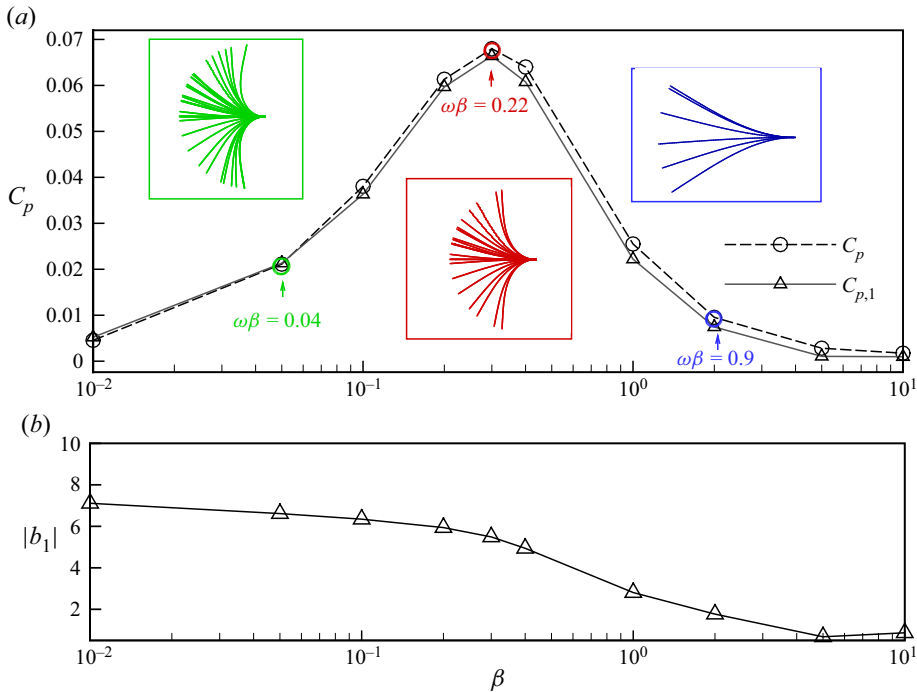


Figure 7. (a) Variation of the energy output C_p and its dominant DMD mode $C_{p,1}$ against β for the moderate flexible lag with $K^* = 0.25$ and $\omega_0 = 0$. The insets show the flag deformation for the cases marked with coloured symbols. (b) Variation of the amplitude of the dominant DMD mode against β .

energy output from each DMD mode can be formulated as

$$C_{p,j} = \frac{2\alpha^2 K^* |b_j|^2}{\beta + \frac{1}{\beta \text{Im}\{\omega_j\}^2}}, \quad (4.1)$$

where $|b_j|$ stands for the amplitude of the j th DMD mode, $\text{Im}\{\omega_j\}$, i.e. the imaginary part of ω_j is the frequency of this mode. The derivation of (4.1) is provided in Appendix B.

As an example, in figure 8(a) we present the DMD spectrum of the case with $\beta = 0.3$, where the energy output C_p achieves its peak value (see figure 7a). It is seen that the dynamics of the excitation term of (3.12) can be represented by the dominant DMD mode, whose amplitude $|b_j| = 12.2$. Its oscillation frequency $\text{Im}\{\omega_j\} = 0.76$ is, not surprisingly, consistent with the flapping frequency of the flag which can be read from figure 6. Figure 8(b) plots the time evolution of Λ at the mid-point ($s = 0.5$) and its reconstruction using the first 10 DMD modes, proving the accuracy of the data decomposition process.

Figure 8(c) further presents the energy contribution of each mode calculated by (4.1). As expected, the leading mode provides the greatest portion of the overall energy generation. Specifically, $C_{p,1}$ (here, the subscript '1' refers to the leading DMD mode) accounts for 91% of the total electrical energy output C_p . Cases in figure 7 with other β values, without any exception, share a similar feature: the overall energy output is mostly attributed to the leading DMD mode. As a result, as displayed in figure 7(a), in which we present C_p and $C_{p,1}$ together, the two quantities are very close to each other over the range of β we consider.

Energy harvesting using an inverted flag with RLC circuit

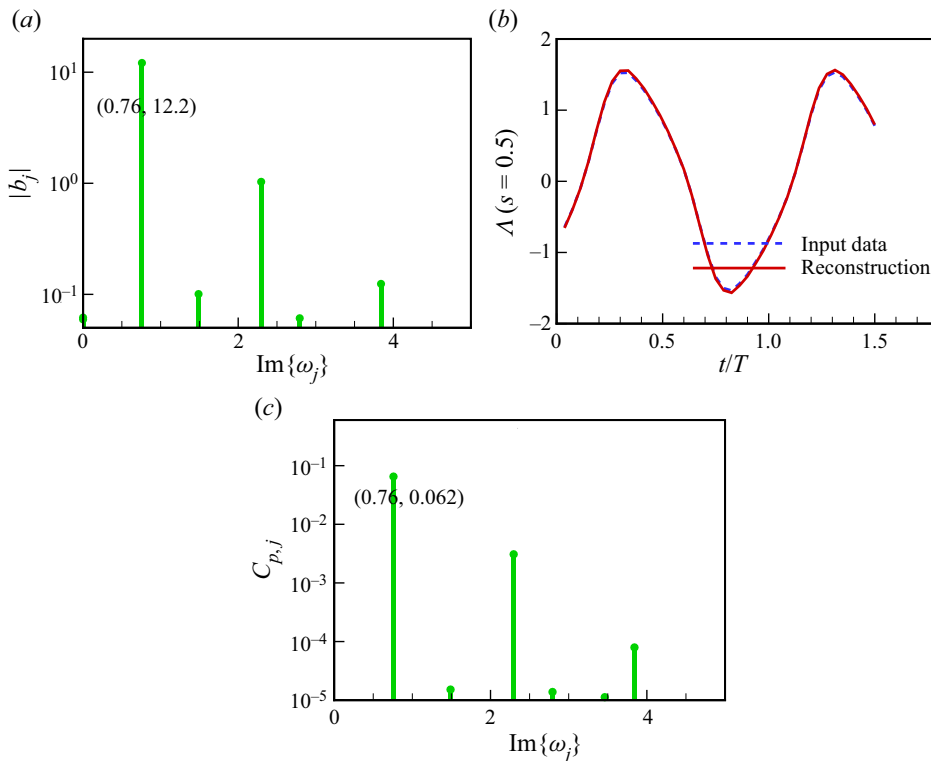


Figure 8. (a) The DMD spectrum of Λ for the case with $\beta = 0.3$. (b) Time history of Λ at the flag mid-point $s = 0.5$ and the reconstruction with the first 10 DMD modes. (c) Energy output $C_{p,j}$ contributed by the DMD modes.

From (4.1), one can see that the energy transfer is mainly determined by three variables, namely the resistance parameter, β , the magnitude, $|b_1|$, and the frequency, $\text{Im}\{\omega_1\}$, of the leading DMD mode of the curvature distribution. Shoele & Mittal (2016) reported that, at $\alpha = 0.5$, where the electromechanical coupling is relatively weak, the flapping amplitude of the flag (which can be approximately reflected by $|b_1|$) remains nearly unchanged over β . Meanwhile, as revealed in figure 6, the flapping frequency ω (approximately represented by the leading frequency $\text{Im}\{\omega_1\}$) usually falls in a much narrower range (between $O(10^{-1})$ and $O(10^0)$) compared with β . Therefore, the optimal energy output C_p (approximately represented by $C_{p,1}$) can be achieved roughly under the condition $\omega\beta \approx \text{Im}\{\omega_1\}\beta = 1$, where the denominator of the right-hand side of (4.1) is minimized while the numerator is constant. This derivation, again, confirms the optimal condition proposed by Michelin & Doaré (2013) and Shoele & Mittal (2016), i.e. $\omega\beta \sim O(1)$. Nevertheless, the strong electromechanical coupling considered in the present study makes $|b_1|$ decrease prominently with β , especially in range of $10^{-1} < \beta < 10$ (see figure 7b), instead of remaining nearly unchanged. This may be responsible for the optimal condition moving towards the lower bound of $O(1)$.

The energy output C_p defined in (3.14) and presented in figure 7(a) is a quantity averaged over the length of the flag. Since the curvature of the fluttering flag is generally non-uniform, the generated energy varies along its length. To compare the contributions from different sections of the flag, we present in figure 9 the distributions of local curvature $\langle |\Lambda| \rangle$ and corresponding local energy output $\langle v^2/\beta \rangle$ along the length of the flag, both

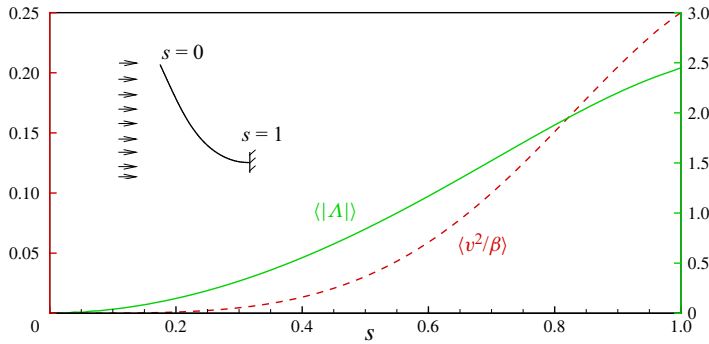


Figure 9. Distributions of the energy output $\langle v^2/\beta \rangle$ and the curvature $\langle |A| \rangle$ along the length of the flag for the case with $\beta = 0.3$, where $\langle \cdot \rangle$ is the time-averaging operator.

being time-averaged quantities, for the case with $\beta = 0.3$. Not surprisingly, they both monotonically increase with s and reach their respective maximum at the trailing edge ($s = 1$), consistent with what has been reported in Singh, Michelin & De Langre (2012) and Piñeirua, Doaré & Michelin (2015). The downstream half of the flag ($0.5 < s < 1$) contributes approximately 90% of the overall energy, suggesting that in practice it is more cost effective to deploy piezoelectric patches only in this part.

4.2.2. The RLC circuit

When an inductor is introduced into the circuit, the circuit becomes an RLC circuit with an undamped natural frequency ω_0 . We have shown in § 4.1 that varying ω_0 may result in mode transitions for the inverted piezohydroelastic flag, which is associated with the ‘lock-in’ phenomenon. In this subsection, we further evaluate its influence on the energy harvesting performance.

Figure 10 presents the variations of the flag energy output C_p against the frequency ratio ω_0/ω at different β values. It is seen that, regardless the flag stiffness, the implementation of small ω_0 (corresponding to very large inductance), e.g. $\omega_0/\omega = 0.1$, makes the circuit close to a pure RC one, so that the energy output remains almost the same as that at $\omega_0 = 0$. On the other hand, very large ω_0 tends to short circuit the loop, resulting in almost zero energy output. Similarly, when the resistance β is too small or too large (e.g. $\beta = 0.01$ or 100), the electrical loop is close to short circuited or a pure inductor-capacitor circuit. In either case the energy output is trivial. As such, the enhancement of energy output from the RLC circuit can only be possible when both ω_0 and β are moderate. Indeed, significant enhancement is observed for both the moderate flexible flag (i.e. $K^* = 0.25$ in figure 10a) and the less flexible flag (i.e. $K^* = 0.4$ in figure 10b), in the ‘lock-in’ regime where $\omega_0/\omega \sim O(1)$. For the moderate flexible flag, however, three exception cases are observed, i.e. $\beta = 0.01, 0.1$ and 0.4, where the electrical circuit is overdamped and hence cannot induce larger structure motions through the ‘lock-in’. For the stiff flag, the performance improvement induced by the ‘lock-in’ seems more pronounced. This is attributed to the extremely low energy output produced in the small ω_0 cases which are mainly in the unfavourable small-deflection mode (evidenced in figures 5 and 6).

Upon closer inspection of figure 10(a,b), it is found that all maximum C_p values (marked with filled symbols) occurring in the RLC-circuit regime (where $\omega_0 \neq 0$) are located slightly to the right of the $\omega_0/\omega = 1$ line due to the damped nature of the circuit. The corresponding optimal frequency ratio $(\omega_0/\omega)_{opt}$ that leads to the maximum

Energy harvesting using an inverted flag with RLC circuit

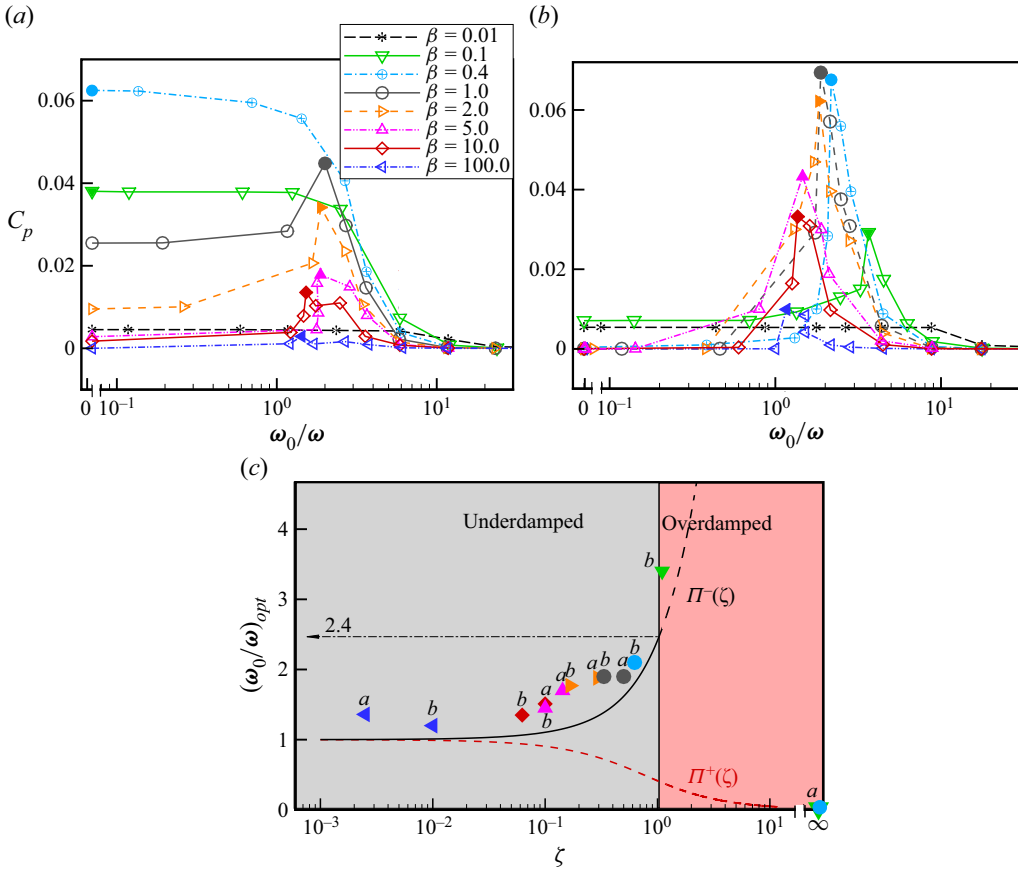


Figure 10. Variation of C_p against ω_0/ω for (a) the moderate flexible flag ($K^* = 0.25$) and (b) the less flexible flag ($K^* = 0.4$). All peaks are marked with filled symbols. (c) Optimal frequency ratio $(\omega_0/\omega)_{opt}$ vs damping ratio ζ . The scatters are $(\omega_0/\omega)_{opt}$ extracted from (a,b).

C_p is expected to be highly associated with the circuit's damping ratio $\zeta = 1/2\beta\omega_0$. As such, we map all these maximum C_p values in the $(\omega_0/\omega)_{opt} - \zeta$ space as shown in figure 10(c). Two sequences of data labelled 'a' and 'b' are respectively extracted from panels (a) and (b). As expected, all these RLC-circuit boosted maximum C_p values appear in the underdamped zone (i.e. $\zeta < 1$). Moreover, all the corresponding optimal frequency ratios are greater than 1, and they generally grow with ζ . In contrast, all the maximum C_p values occurring in the RC-circuit regime (where $\omega_0 = 0$) are located at the same place in the overdamped zone (i.e. $\zeta > 1$), where $\zeta = +\infty$ and $(\omega_0/\omega)_{opt} = 0$.

To establish a better understanding of the optimal performance of the system, the DMD analysis is also conducted for the flag equipped with oscillatory circuits. We present in figure 11 the DMD analysis results of a representative sequence of cases with various ω_0 and $\beta = 1.0$ for the moderate flexible flag, which specifies the spectrum and energy output of the leading few DMD modes (calculated with (B11)), and compares the total energy output C_p with the contributions from the first two DMD modes. As revealed in (a-e), when ω_0 is small the energy output is dominated by the leading mode. However, as ω_0 exceeds 1.0 the energy output of the second modes (appearing at the third harmonic

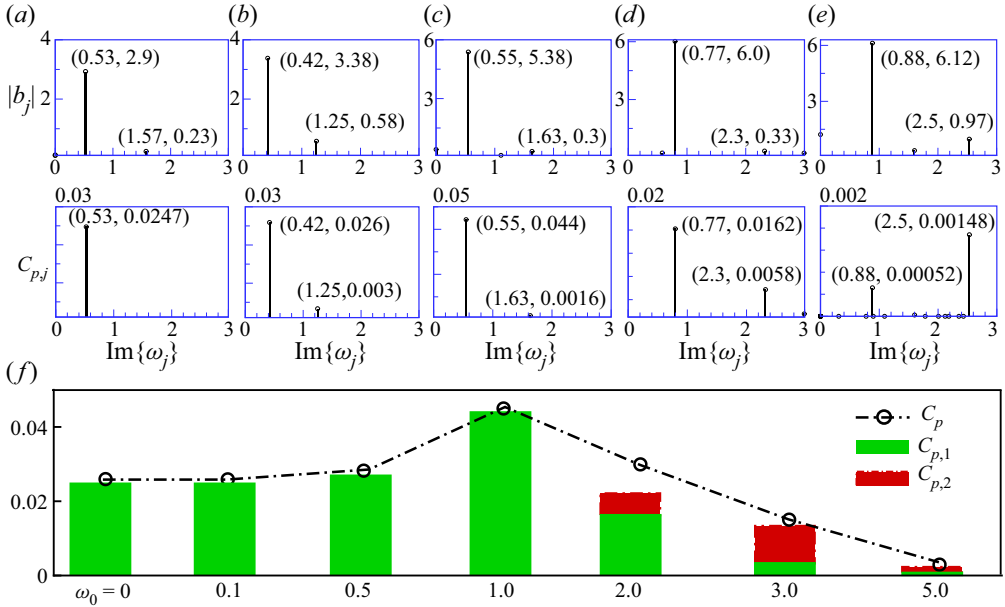


Figure 11. (a–e) The DMD spectra of the flag energy harvesting process and the corresponding energy output for different ω_0 when $\beta = 1.0$ and $K^* = 0.25$. (f) Total energy output C_p and contributions from the first or two DMD modes vs ω_0 . Panels show (a) $\omega_0 = 0$, (b) $\omega_0 = 0.5$, (c) $\omega_0 = 1.0$, (d) $\omega_0 = 2.0$, (e) $\omega_0 = 5.0$.

frequency) significantly increases, which can be even higher than the first mode (e.g. at $\omega_0 = 5.0$ in e). As such, in this ω_0 regime the electrical dynamics is determined by the coupled effect of the first few modes, instead of solely by the leading mode. It is necessary to point out that, when higher frequency modes play a considerable role in the electrical dynamics, the linear combination of $C_{p,1}$ and $C_{p,2}$ may not reproduce C_p exactly. This is because when there are multiple modes of the same order of magnitude contributing to the energy output, the interaction among these modes could be strong and hence cannot be neglected. Nevertheless, in the ‘lock-in’ regime where ω_0 is near or less than 1.0, the leading DMD mode still plays a dominant role in contributing to C_p .

With the above observation, it is inferred that the $C_{p,1}$ formulation is still useful in determining the condition for optimal energy output. According to Appendix B, we have

$$C_{p,1} \sim \frac{\alpha^2 K^*}{\beta \left(\frac{\omega_0^2}{\text{Im}\{\omega_1\}^2} - 1 \right)^2 + \frac{1}{\beta \text{Im}\{\omega_1\}^2}} |b_1|^2. \quad (4.2)$$

As noted before, the amplitude $|b_1|$ and frequency $\text{Im}\{\omega_1\}$ of the leading DMD mode vary slightly in comparison with β in the ‘lock-in’ regime. The denominator of the above formula is minimized approximately when

$$\beta \left(\frac{\omega_0^2}{\text{Im}\{\omega_1\}^2} - 1 \right)^2 \approx \frac{1}{\beta \text{Im}\{\omega_1\}^2}, \quad (4.3)$$

Energy harvesting using an inverted flag with RLC circuit

which can be rewritten as $\text{Im}\{\omega_1\}^4 - (2\omega_0^2 + 1/\beta^2)\text{Im}\{\omega_1\}^2 + \omega_0^4 \approx 0$. Solving it gives

$$\text{Im}\{\omega_1\}^2 \approx \omega_0^2 \left(1 + 2\zeta^2 \pm 2\zeta\sqrt{1 + \zeta^2} \right), \quad (4.4)$$

where $\zeta = 1/(2\beta\omega_0)$ is the damping ratio of the electrical circuit. We obtain a simple expression of the optimal frequency ratio that leads to the maximum energy output

$$\left(\frac{\omega_0}{\omega} \right)_{opt} \approx \frac{1}{\sqrt{1 + 2\zeta^2 \pm 2\zeta\sqrt{1 + \zeta^2}}} = \Pi(\zeta). \quad (4.5)$$

If plotting (4.5) by adopting the negative sign in figure 10(c), we see all the optimal frequency ratios appearing in the RLC-circuit regime (see figure 10a,b) are located near the prediction (the black solid curve) in the underdamped zone, following a similar trend. Due to the damping effect exerted by the circuit on the flag dynamics, all these values are located above the prediction curve. It is interesting to see that (4.5), if adopting the positive sign, also captures all the optimal frequency ratios appearing in the RC-circuit regime, even though they collapse at the same point in the overdamped zone. Overall speaking, (4.5) provides a fairly good prediction of the optimal frequency for the electrohydroelastic flag where the electrical damping ratio is known.

Although very insightful, (4.5) includes the system response frequency ω , which is unknown beforehand. To better facilitate the selection of electrical circuit for energy harvesting, especially when the electrical load (β) is known and the inductance (ℓ or ω_0) is to be determined, C_p contours for the moderate and less flexible flags are plotted in the $\omega_0 - \beta$ space, as shown in figure 12(a,b), respectively, in which all the optimal cases (with maximum C_p for given β) are marked with red circles. To underline the potential of performance enhancement by using RLC circuits, figure 12(c,d) further compare the maximum C_p values at various β when the RC or RLC circuit is deployed, which are extracted from the contours. Obviously, at lower β (the range varies with the stiffness of the flag), the maximum C_p is achieved with RC circuits, indicating that the employment of an inductor fails to improve the system performance. At higher β , on the contrary, the best performance is achieved by RLC circuits (i.e. with non-zero ω_0) through the ‘lock-in’. The boundary that separates these two optimal regimes, as shown in the figure, is the $\zeta = 1.0$ (the critical damping) line. The implication is that, to trigger the ‘lock-in’ state, one should carefully choose the inductance ω_0 to ensure the damping ratio falls into the underdamped zone, i.e. $\omega_0 > 1/2\beta$, which defines the lower bound of the optimal ω_0 .

It is also observed from figure 12 that, in the underdamped zone (i.e. $\zeta < 1$), the maximum C_p generally decreases with β despite some local peak or plateau. This suggests a possible upper bound for the optimal ω_0 . From (4.5), we can obtain in the underdamped zone the maximum value of optimal ω_0/ω , i.e. $\max(\omega_0/\omega)_{opt} \approx 2.4$, which corresponds to the intersection point value of the (4.5) curve and the $\zeta = 1$ line, as denoted in figure 10(c). Note that, when undergoing the flutter modes, the flapping frequency of the electrohydroelastic flag ω is upper bounded by the frequency of the pure mechanical flag ω_s , i.e. $\omega < \omega_s$, which is evidenced in figure 6(a,c). This leads to a reasonable upper bound for optimal ω_0 , i.e. $\omega_0 < 2.4\omega_s$. Therefore, the optimal ω_0 shall be chosen in a double-bounded range as

$$0.5\beta^{-1} < \omega_0 < 2.4\omega_s. \quad (4.6)$$

This bounded range is depicted by the triangle zone formed with the two black dashed lines shown in figure 12(a,b). Note that some optimal ω_0 value slightly falls outside this

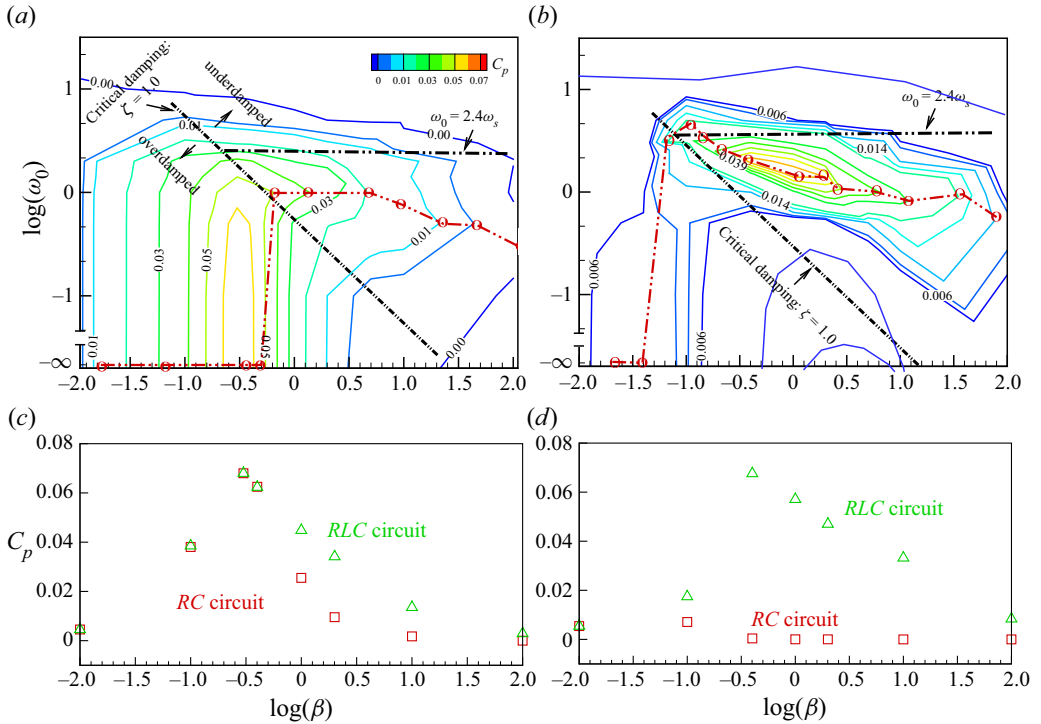


Figure 12. (a,b) Contour map of C_p in the $\beta - \omega_0$ space and (c,d) comparison of C_p between the optimal RLC circuit (extracted from the contour maps along the red trajectories) and the RC circuit: (a,c) the moderate flexible flag and (b,d) the less flexible flag. Panels show (a) $K^* = 0.25$, (b) $K^* = 0.4$, (c) $K^* = 0.25$, (d) $K^* = 0.4$.

triangle zone, especially near the $\zeta = 1$ line (see figure 12b). This can be attributed to the general underestimation made by (4.5) through ignoring the damping the circuit brings to the electrohydroelastic flag. Nevertheless, the bounded range described by (4.6) still delineates an acceptable zone for optimal ω_0 .

Note that (4.6) requires a condition

$$\beta > 0.21\omega_s^{-1}. \tag{4.7}$$

It indicates that, if one would like to utilize RLC circuits to achieve better performance over RC circuits, the electrical load β must be greater than a critical value, i.e. $0.21\omega_s^{-1}$. Otherwise, the use of RLC circuits cannot bring any benefit.

The optimal frequency ratio (4.5), the proposed searching zone for the optimal ω_0 (4.6) and the critical electrical load (4.7) are very useful in guiding the optimization process of the electrical circuits. They can assist in choosing an appropriate inductor quickly and efficiently when RLC circuits are needed for higher energy production, which usually happens at relatively large electrical load.

It should be pointed out that, although the free-stream velocity U^* is not explicitly adopted as a design variable in the above optimization process, its influence has already been reflected in (4.5)–(4.7). Specifically, in (4.5) it affects ω , the actual response frequency of the system, through complex fluid–structure–electric coupling, whereas in (4.6) and (4.7) it affects the ranges of ω_0 and β through ω_s , the flutter frequency of the pure mechanical flag.

5. Conclusions and discussion

The present study focuses on the multi-physics dynamics of an inverted electrohydroelastic flag. The mechanical energy of ambient flows is harvested through FIV, which is then converted into electricity via an electric circuit. By using a fully coupled fluid–structure–electric model, we simulate the entire energy conversion process, with the focus placed on the dynamics of the flag and its energy output, particularly the impacts of structural and electrical parameters.

Via parametric studies, a variety of structural response modes are identified. Among these response modes, the two flutter modes, i.e. the symmetric- and asymmetric-flutter modes, are the most suitable ones for sustainable energy harvesting. We found that, with moderate flexibility, the flag is more likely to fall into the flutter modes, whereas too flexible flags can be easily bent and deflected to one side considerably (large-deflection mode) and too rigid flags tend to remain almost undeformed (small-deflection mode). We also found that, with only an RC circuit deployed, the increase of electrical load (i.e. β) can stabilize the flag.

For benchmark purposes, the energy harvesting performance of the flag equipped with an RC circuit is first examined. Our simulation results and DMD-analysis-based derivations confirm the optimal condition, i.e. $\beta\omega \sim O(1)$, for the maximum energy output. However, unlike in the weak electromechanical coupling scenario, where this optimal condition works very well, the strong coupling considered in the present study connotes more complicated nonlinear fluid–structure–electric interaction and pushes this condition towards the lower bound of $O(1)$.

We then proceed to study the impact of inductors on the performance of the system. By adding an inductor, the output loop becomes an oscillatory RLC circuit with an undamped natural frequency ω_0 . Our results show that, when the circuit's natural frequency ω_0 satisfies $0.5\beta^{-1} < \omega_0 < 2.4\omega_s$ (i.e. (4.6)), the employment of the oscillatory circuit tends to lock the structural vibration frequency into the circuit's frequency, which can significantly improve the energy harvesting performance. This performance improvement due to the 'lock-in' can only occur in the underdamped zone. Furthermore, the optimal ω_0 can be estimated by (4.5). These findings and guidelines are expected to play an important role in the RLC circuit design and optimization.

In the present study, an RLC circuit is used to harvest the energy from ambient flows. However, we note that the simplified electrical rendition is still far from the real system to be developed. For example, for voltage compatibility, electrical interfaces need to be applied between the terminal electric load and the piezoelectric element (Sarker *et al.* 2019). The most frequently used interface is the combination of a diode rectifier bridge and a filter capacitor, which are respectively used for rectifying and smoothing the alternating voltage (Lefeuvre *et al.* 2006). Moreover, more complicated interfaces based on the so-called synchronized switching harvesting with inductor technique based on a specific nonlinear processing of the voltage have been proposed (Daniel *et al.* 2016; Li, Roy & Calhoun 2019). Such interfaces can significantly affect the dynamics of the flag and influence the energy output. Therefore, a complete multi-physics model that involves an electric interface may be a better option, whose results can be directly used for guiding the prototype development. This will be our future direction in this area.

Funding. This work was supported by Research Grants Council of Hong Kong under General Research Fund (grant number 15218421); the Hong Kong Polytechnic University Shenzhen Research Institute (grant number J2023A011); and the Hong Kong Polytechnic University under Postdoc Matching Fund Scheme (X.B., grant number W211).

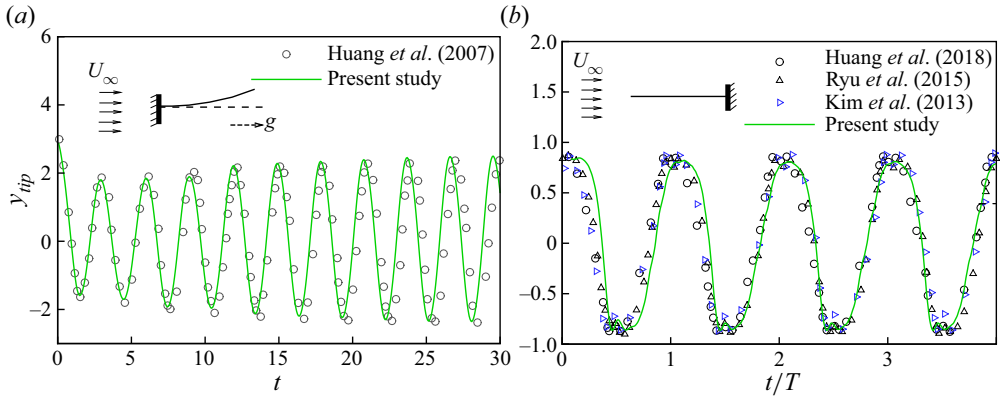


Figure 13. (a) Time histories of vertical displacement of the regular flag’s tip: $Re = 300, m^* = 1.0, K^* = 0.001, Fr = 0.5$. (b) Time histories of the vertical displacement of the inverted flag: $Re = 250, m^* = 1.0, K^* = 0.25$.

Declaration of interests. The authors report no conflict of interest.

Author ORCIDs.

- Chenglei Wang <https://orcid.org/0000-0003-0771-8667>;
- Qiang Zhu <https://orcid.org/0000-0003-1048-1357>;
- Hui Tang <https://orcid.org/0000-0002-6774-507X>.

Appendix A. Validation of the numerical model

A.1. Validation of the fluid–structure interaction solver

We verify the accuracy of the fluid–structure interaction solver with two canonical tests. The first one is the relaxation test of a conventional cantilevered filament (whose trailing edge is free and the leading edge is fixed) in an axial flow. The second test is to simulate the flow-induced flutter motion of an inverted cantilevered flag in an incoming flow. Both tests are performed by setting the electromechanical coupling factor α to zero to remove the influence of the electrical circuit.

For the first test, the initial state of the filament is defined by the equation

$$X_{j-1} = X_j - \Delta s[\cos((N - j)a), -\sin((N - j)a)], \quad V_j = 0, \quad j = N, N - 1, \dots, 2, \tag{A1}$$

where a is a small number (here, we choose $a = 0.01$), N is number of Lagrangian nodes along s . Note that the trailing end of the flag is fixed, i.e. $X_1 = V_1 = 0$. Released from the strained configuration described by (A1), the motion of the conventional filament under the effects of the fluid field and gravity is then examined using our fluid–structure interaction model at $Re = 300, m^* = 1.0, K^* = 0.001, Fr = 0.5$ (Froude number). The lateral position of the tip y_{tip} is measured throughout the vibration. As displayed in figure 13(a), our simulation perfectly reproduces the time evolution of the tip motion reported in a previous numerical experiment (Huang *et al.* 2007). In the second test, induced by the fluid instability the inverted cantilever flag displays self-sustained flutter motion with a certain frequency. As shown in figure 13(b), the present study acquires nearly identical motion amplitude and frequency as existing numerical and experimental works (Kim *et al.* 2013; Ryu *et al.* 2015; Huang, Wei & Lu 2018). Therefore the two tests prove our hydroelastic solver is accurate and robust.

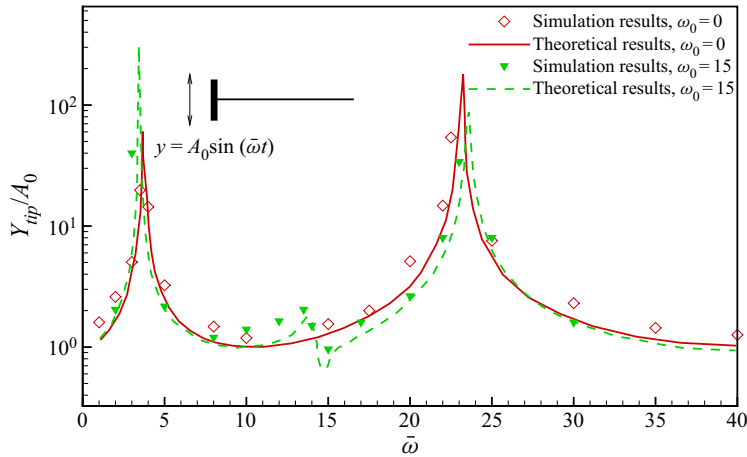


Figure 14. Spectrum of the amplification factor at the tip of the piezoelectric flag as functions of the actuation frequency $\bar{\omega}$, $m^* = 1.0$, $K^* = 1.0$, $\alpha = 0.3$, $\beta = 1.0$.

A.2. Validation of the structure–electrical model

A.2.1. Forced vibration of a piezoelectric flag

The validity of the structure–electric model is firstly assessed with a canonical case, in which a cantilever piezoelectric flag experiences forced vibration in the absence of the ambient flow. Following Shoole & Mittal (2016), the flag vibration is driven by the prescribed periodic heaving motion of the fixed end: $y_0 = A_0 \sin(\bar{\omega}t)$, in which A_0 is a sufficiently small amplitude catering to the small-deflection assumption so that nonlinearities can be neglected. Here, it is chosen to be $0.002L$. Assuming the vertical displacement of the flag $y(s, t) = \text{Re}[Y(s)e^{i\omega t}]$ and the generated voltage $v(s, t) = \text{Re}[V(s)e^{i\omega t}]$, we then conduct modal analysis on the piezoelectric equations (3.12), yielding

$$\frac{d^4 Y}{ds^4} - \kappa(\omega)^4 Y = 0, \tag{A2}$$

in which

$$\kappa(\omega) = \sqrt[4]{\frac{\omega^2}{m^* K^*} \left[1 - \frac{\beta \alpha^2 \omega}{\beta(\omega_0^2 - \omega^2) + i\omega} \right]^{-1}}. \tag{A3}$$

By solving the above equation with boundary conditions, the deflection of the free end is formulated as

$$Y_{tip} = \frac{\cos(\kappa(\bar{\omega})) + \cosh(\kappa(\bar{\omega}))}{\cos(\kappa(\bar{\omega})) \cosh(\kappa(\bar{\omega})) + 1}. \tag{A4}$$

Herein, the forced vibration is simulated with our structure–electric model for two different electrical circuits, i.e. RC ($\omega_0 = 0$) and RLC ($\omega_0 = 15$). Other electrical and mechanical parameters are fixed at $m^* = 1.0$, $K^* = 1.0$, $\alpha = 0.3$, $\beta = 1.0$. In figure 14 we compare the simulation results with the theoretical prediction obtained by (A4). It shows that the simulations are able to capture the natural frequencies of the piezoelectric flag. Note that the implementation of the inductor is found to have negligible impacts on the tip deflection, except for the enlarged damping effect that happens when the excitation

frequency coincides the circuit's natural frequency (see the trough in the figure at $\omega_0 = 15$). Our structure–electrical model successfully predicts the damping phenomenon.

A.2.2. Free vibration of a simply supported piezoelectric beam

We then proceed to assess the structure–electrical model's accuracy through a relaxation test, the free vibration of a piezoelectric beam with both ends simply supported. Only with this specific boundary condition is it possible to analytically solve the piezoelectric equations with finite Fourier transform. Using the small-deflection assumption, (3.12) is linearized as

$$\left. \begin{aligned} \frac{\partial^2 y}{\partial t^2} &= -m^* K^* \frac{\partial^4 y}{\partial s^4} + \alpha m^* \sqrt{K^*} \frac{\partial^2 v}{\partial s^2}, \\ \beta \frac{\partial^2 v}{\partial t^2} + \frac{\partial v}{\partial t} + \beta \omega_0^2 v &= -\alpha \beta \sqrt{K^*} \frac{\partial^4 y}{\partial t^2 \partial s^2} \end{aligned} \right\}, \tag{A5}$$

and the boundary conditions are $y = 0, \partial^2 y / \partial s^2 = \alpha v / \sqrt{K^*}$ at $s = 0$ or $s = 1$. Solutions of the above linear system can be written as

$$y(s, t) = 2 \sum_{n=1}^{\infty} \hat{y}(n, t) \sin(n\pi s), \quad v(s, t) = 2 \sum_{n=1}^{\infty} \hat{v}(n, t) \sin(n\pi s), \tag{A6a,b}$$

in which the coefficients are given by

$$\hat{y}(n, t) = \int_0^1 y(s, t) \sin(n\pi s) ds, \quad \hat{v}(n, t) = \int_0^1 v(s, t) \sin(n\pi s) ds. \tag{A7a,b}$$

We multiply (A5) by $\sin(n\pi s)$ and integrate with respect to s from 0 to 1, yielding

$$\left. \begin{aligned} \frac{\partial^2 \hat{y}}{\partial t^2} + m^* K^* n^4 \pi^4 \hat{y} &= -\alpha m^* \sqrt{K^*} n^2 \pi^2 \hat{v}, \\ \beta \frac{\partial^2 \hat{v}}{\partial t^2} + \frac{\partial \hat{v}}{\partial t} + \beta \omega_0^2 \hat{v} &= \alpha \beta \sqrt{K^*} n^2 \pi^2 \frac{\partial^2 \hat{y}}{\partial t^2}. \end{aligned} \right\} \tag{A8}$$

We take the solutions of the eigenvalue problem as $\hat{y} = \hat{Y} e^{i\omega_n t}$ and $\hat{v} = \hat{\Upsilon} e^{i\omega_n t}$ and substitute into (A8), yielding

$$\left. \begin{aligned} (-\omega_n^2 + m^* K^* n^4 \pi^4) \hat{Y} + \alpha m^* \sqrt{K^*} n^2 \pi^2 \hat{\Upsilon} &= 0, \\ (-\beta \omega_n^2 + i\omega_n + \beta \omega_0^2) \hat{\Upsilon} + \alpha \beta \sqrt{K^*} n^2 \pi^2 \omega_n^2 \hat{Y} &= 0. \end{aligned} \right\} \tag{A9}$$

The equation can be further reduced to the characteristic equation of the eigenvalue problem

$$\begin{aligned} \beta \omega_n^4 - i\omega_n^3 - \beta \left(m^* K^* n^4 \pi^4 (1 + \alpha^2) + \omega_0^2 \right) \omega_n^2 + i m^* K^* n^4 \pi^4 \omega_n \\ + \beta \omega_0^2 m^* K^* n^4 \pi^4 = 0. \end{aligned} \tag{A10}$$

Each solution $\omega_{n,j}$ ($j = 1, 2, 3, 4$) of the fourth-order polynomial equation corresponds to a normal mode vector

$$\begin{pmatrix} \hat{Y}^{(j)} \\ \hat{\Upsilon}^{(j)} \end{pmatrix} e^{i\omega_{n,j} t} = \begin{pmatrix} \hat{Y}^{(j)} \\ r^{(j)} \hat{Y}^{(j)} \end{pmatrix} e^{i\omega_{n,j} t}, \tag{A11}$$

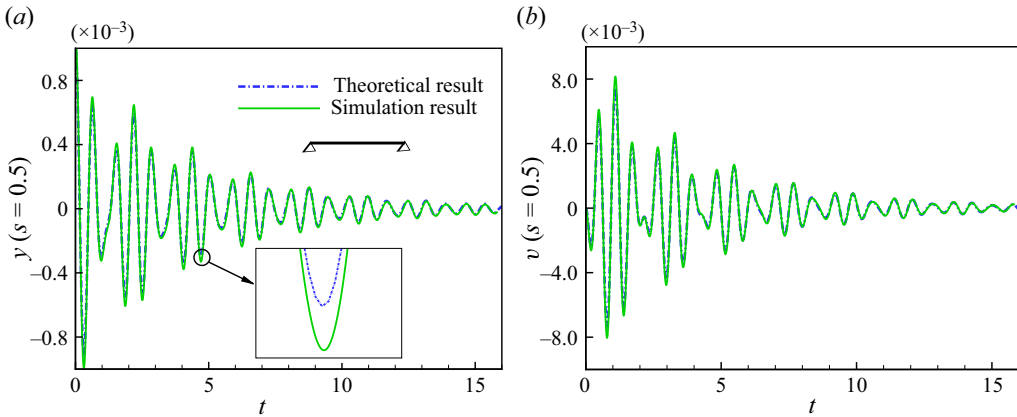


Figure 15. Time histories of the (a) deflection and (b) electric voltage at the centroid of the beam ($s = 0.5$), $\alpha = 0.3$, $\omega_0 = 10$, $\beta = K^* = m^* = 1.0$.

in which $r^{(j)}$ is obtained by substituting $\omega_{n,j}$ into (A9), leading to

$$r^{(j)} = \frac{\omega_{n,j}^2 - m^* K^* n^4 \pi^4}{\alpha \sqrt{K^* m^* n^2 \pi^2}}. \tag{A12}$$

Thus, the general solution to (A8) is calculated by the linear superposition of the four normal modes $\hat{y}(n, t) = \sum_{j=1}^4 \hat{Y}^{(j)} e^{i\omega_{n,j}t}$ and $\hat{v}(n, t) = \sum_{j=1}^4 r^{(j)} \hat{Y}^{(j)} e^{i\omega_{n,j}t}$, where the four unknowns $\hat{Y}^{(j)}$ can be determined from initial conditions: $y(s, t = 0) = y_0(s)$, $v(s, t = 0) = v_0(s)$, $dy/dt(s, t = 0) = \dot{y}_0(s)$ and $dv/dt(s, t = 0) = \dot{v}_0(s)$. The finite Fourier sine transforms of the initial conditions yield

$$\left. \begin{aligned} \hat{y}(n, t = 0) &= \int_0^1 y_0(s) \sin(n\pi s) ds, \\ \frac{d\hat{y}}{dt}(n, t = 0) &= \int_0^1 \dot{y}_0(s) \sin(n\pi s) ds, \\ \hat{v}(n, t = 0) &= \int_0^1 v_0(s) \sin(n\pi s) ds, \\ \frac{d\hat{v}}{dt}(n, t = 0) &= \int_0^1 \dot{v}_0(s) \sin(n\pi s) ds. \end{aligned} \right\} \tag{A13}$$

Finally, the solutions of (A5) can be calculated by substituting $\hat{y}(n, t)$ and $\hat{v}(n, t)$ into (A6a,b).

Here, we set $y_0(s) = a \sin(\pi s)$ ($a = 0.001$) and $\dot{y}_0 = v_0 = \dot{v}_0 = 0$, such that all modes except for the first one disappear due to the orthogonality of trigonometric functions. The solutions turn out to be $y(s, t) = 2 \sum_{j=1}^4 \hat{Y}^{(j)} e^{i\omega_{1,j}t} \sin(\pi s)$ and $v(s, t) = 2 \sum_{j=1}^4 r^{(j)} \hat{Y}^{(j)} e^{i\omega_{1,j}t} \sin(\pi s)$. In figure 15 we compare our numerical predictions of $y(0.5, t)$ and $v(0.5, t)$ (measured at the beam centroid) with the analytical solutions for the case of $\alpha = 0.3$, $\omega_0 = 10$, $\beta = K^* = m^* = 1.0$. As is shown in the figure, the numerical results are in good agreement with the theoretical analysis, verifying the validity of our piezoelectric model.

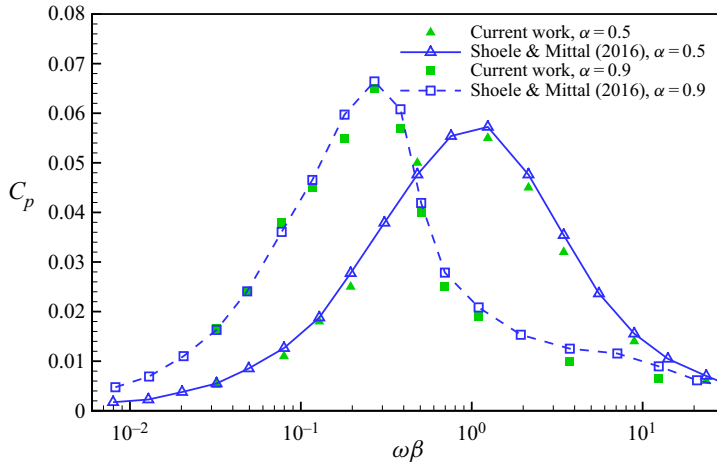


Figure 16. Energy harvesting efficiency C_p as functions of the product of the structural frequency ω and the tuning coefficient β when $\omega_0 = 0$, $K^* = 0.25$, $m^* = 1$.

A.3. Validation of the entire piezohydroelastic model

Having verified the robustness of the two ‘submodules’ (i.e. the fluid–structure and structure–electrical interactions), we then focus on the whole fluid–structure–electrical model in this section. The energy harvesting capability of the piezohydroelastic system with purely resistive circuit is evaluated at various electroelastic coupling coefficients α and tuning coefficients β . As shown in figure 16, the efficiencies predicted by our model are in perfect accord with the simulation data from the reference (Shoele & Mittal 2016), proving that the piezohydroelastic model is reliable and accurate.

Appendix B. Dynamic mode decomposition of the mechano-electrical system

Dynamic mode decomposition (Kutz *et al.* 2016) is a data decomposition method that serves to extract a coherent relevant data structure and its temporal dynamics (e.g. growth rate and frequency) from a sequence of discrete data. In our case the variable of interest is the local curvature Λ , thus a time series of Λ with equal time interval ΔT is synthesized into a matrix as

$$\Lambda_1^m = \begin{bmatrix} | & | & \cdots & | \\ \Lambda_1 & \Lambda_2 & \cdots & \Lambda_m \\ | & | & & | \end{bmatrix}, \tag{B1}$$

where m is the number of time snapshots and each column represents the discrete distribution of Λ along the flag for each snapshot, e.g.

$$\Lambda_1 = \begin{bmatrix} \Lambda_1(\Delta s) \\ \Lambda_1(2\Delta s) \\ \vdots \\ \Lambda_1(N\Delta s) \end{bmatrix}, \tag{B2}$$

in which Δs is the spatial interval corresponding to the Lagrangian grid size, and N is the size of the vector. Even though those snapshots are normally obtained from a nonlinear process, DMD aims to find an optimal linear operator \mathcal{A} to achieve inter-snapshot linear mapping between any two consecutive snapshots, i.e. $\Lambda_{i+1} = \mathcal{A} \Lambda_i$. Physically, this

process can be interpreted as the linear-tangent approximation of a nonlinear dynamic. Given the constant mapping between the snapshots, the operator \mathcal{A} becomes a linear mapping from data sequence Λ_1^{m-1} to Λ_2^m :

$$\Lambda_2^m = \{\Lambda_2, \Lambda_3, \dots, \Lambda_m\} = \mathcal{A} \{\Lambda_1, \Lambda_2, \dots, \Lambda_{m-1}\} = \mathcal{A} \Lambda_1^{m-1} \tag{B3}$$

$$\mathcal{A} = \Lambda_2^m \cdot (\Lambda_1^{m-1})^\dagger. \tag{B4}$$

The DMD computes the leading eigendecomposition of \mathcal{A} to obtain the dynamic modes (ϕ) and their corresponding eigenvalues (λ).

With eigenvalues and eigenvectors of \mathcal{A} determined, the curvature distribution of arbitrary snapshot at time $t_k = k\Delta T$ can be reconstructed by

$$\Lambda(t_k) = \sum_{j=0}^m b_j \lambda_j^{k-1} \phi_j, \tag{B5}$$

where b_j denotes the magnitude of the discrete mode ϕ_j . λ, ϕ and b_j are all complex quantities. Since the sampled curvature is real, the complex eigenvalues and eigenmodes will be conjugated, thus the imaginary part will disappear in doing above summation.

A continuous projected solution may be derived from the above discrete expression. By assuming $\omega_j = \ln(\lambda_j)/\Delta T$, continuous time evolution of the problem is then given by

$$\Lambda(t) = \sum_{j=0}^m b_j e^{\omega_j t} \phi_j. \tag{B6}$$

The real part of ω_j represents exponential growth or decay rate, and the imaginary part contains the temporal frequency. Due to the periodicity of the structural deformation the growth rate should be negligible, i.e. $\text{Re}\{\omega_j\} \approx 0$. Plugging (B6) into the electrical governing equation (3.12) yields

$$\frac{\partial^2 v}{\partial t^2} + \frac{1}{\beta} \frac{\partial v}{\partial t} + \omega_0^2 v = -\alpha \sqrt{K^*} \sum_j b_j \text{Im}\{\omega_j\}^2 e^{\text{Im}\{\omega_j\}it} \phi_j. \tag{B7}$$

In damped systems, the oscillation in the natural frequency is usually damped out rapidly and only the steady state solution is left. The voltage output of one arbitrary mode ϕ_j at $s_t = t \Delta s$ is

$$v_j(s_t, t) = \frac{-\alpha \sqrt{K^*} b_j \text{Im}\{\omega_j\}^2 \phi_j(s_t)}{\omega_0^2 - \text{Im}\{\omega_j\}^2 + \frac{\text{Im}\{\omega_j\}}{\beta} i} e^{\text{Im}\{\omega_j\}it}, \tag{B8}$$

whose imaginary component can be zeroed out by summing its conjugate counterpart. The real part can be expressed by

$$\text{Re} \{ v_j(s_t, t) \} = -2\hat{v}_j |\phi_j(s_t)| \cos(\text{Im}\{\omega_j\}t + \theta_1 + \theta_2(s_t) - \theta_3), \tag{B9}$$

where

$$\hat{v}_j = \frac{\alpha \sqrt{K^*} \text{Im}\{\omega_j\}^2}{\sqrt{(\text{Im}\{\omega_j\}^2 - \omega_0^2)^2 + \frac{\text{Im}\{\omega_j\}^2}{\beta^2}}} |b_j|, \tag{B10}$$

where the operator $|\cdot|$ calculates the magnitude of the complex number, $\theta_1, \theta_2(s_t)$ and θ_3 represent the argument of $b_j, \phi_j(s_t)$ and $\omega_0^2 - \text{Im}\{\omega_j\}^2 + (\text{Im}\{\omega_j\}/\beta)i$, respectively.

Thus the energy output sourced from a pair of conjugate modes is

$$C_{p,j} \approx \frac{4\hat{v}_j^2}{\beta} \sum_{i=1}^N \left[|\phi_j(s_i)|^2 \int_T \cos^2[\text{Im}\{\omega_j\}t + \theta_1 + \theta_2(s_i) - \theta_3] dt/T \right] \Delta s = \frac{2\hat{v}_j^2 \Delta s}{\beta}, \quad (\text{B11})$$

in which $T = 2\pi/\text{Im}\{\omega_j\}$. Note that the modulus of each mode equals to unity, i.e.

$$\sum_{i=1}^N |\phi_j(s_i)|^2 = 1, \quad s_i = i \Delta s. \quad (\text{B12})$$

Assuming that the spatial equation $\Phi_j(s)$ is the continuous mode corresponding to $\phi_j(s_i)$, one can obtain

$$\int_0^1 |\Phi_j(s)|^2 ds \approx \sum_{i=1}^N |b_j|^2 |\phi_j(s_i)|^2 \Delta s = |b_j|^2 \Delta s = |b_j|^2/N. \quad (\text{B13})$$

Since the left-hand side of the above equation is a constant for a given case, $|b_j|^2$ should be proportional to $1/\Delta s$ (i.e. N). As a result, $C_{p,j}$ is proven to be independent to the sampling interval Δs (or N) after a close inspection of (B10) and (B11). To avoid confusion, in the following $|b_j|^2/N$ will be only presented as a normalized term $|b_j|^2$.

Within a certain DMD framework, C_p^j scales with \hat{v}_j^2/β , which is calculated by

$$\frac{\hat{v}_j^2}{\beta} = \frac{\alpha^2 K^* \text{Im}\{\omega_j\}^4}{\beta (\text{Im}\{\omega_j\}^2 - \omega_0^2)^2 + \frac{\text{Im}\{\omega_j\}^2}{\beta}} |b_j|^2. \quad (\text{B14})$$

Specifically, when the inductive element is absent ($\omega_0 = 0$), we have

$$\frac{\hat{v}_j^2}{\beta} = \frac{\alpha^2 K^* |b_j|^2}{\beta + \frac{1}{\beta \text{Im}\{\omega_j\}^2}}. \quad (\text{B15})$$

REFERENCES

- ABDELKEFI, A., NAYFEH, A.H. & HAJJ, M.R. 2012 Modeling and analysis of piezoaeroelastic energy harvesters. *Nonlinear Dyn.* **67**, 925–939.
- ADHIKARI, S., RASTOGI, A. & BHATTACHARYA, B. 2020 Piezoelectric vortex induced vibration energy harvesting in a random flow field. *Smart Mater. Struct.* **29** (3), 035034.
- AKCABAY, D.T. & YOUNG, Y.L. 2012 Hydroelastic response and energy harvesting potential of flexible piezoelectric beams in viscous flow. *Phys. Fluids* **24**, 054106.
- ALBEN, S. & SHELLEY, M.J. 2008 Flapping states of a flag in an inviscid fluid: bistability and the transition to chaos. *Phys. Rev. Lett.* **100** (7), 074301.
- BARRERO-GIL, A., ALONSO, G. & SANZ-ANDRES, A. 2010 Energy harvesting from transverse galloping. *J. Sound Vib.* **329** (14), 2873–2883.
- BI, X. & ZHU, Q. 2019 Fluid–structure investigation of a squid-inspired swimmer. *Phys. Fluids* **31**, 101901.
- BIBO, A. & DAQAQ, M.F. 2013 Energy harvesting under combined aerodynamic and base excitation. *J. Sound Vib.* **332**, 5086–5102.
- BISEGNA, P., CARUSO, G. & MACERI, F. 2006 Optimized electric networks for vibration damping of piezoactuated beams. *J. Sound Vib.* **289** (4–5), 908–937.
- BONELLO, P. & RAFIQUE, S. 2011 Modeling and analysis of piezoelectric energy harvesting beams using the dynamic stiffness and analytical modal analysis methods. *J. Vib. Acoust.* **133**, 011009–011020.

Energy harvesting using an inverted flag with RLC circuit

- CERDEIRA, C.H., GOZA, A., SADER, J.E., COLONIUS, T. & GHARIB, M. 2021 Dynamics of an inverted cantilever plate at moderate angle of attack. *J. Fluid Mech.* **909**, A20.
- CONNELL, B.S.H. & YUE, D.K.P. 2007 Flapping dynamics of a flag in a uniform stream. *J. Fluid Mech.* **581**, 33–67.
- CROSS, E. 2004 Materials science: lead-free at last. *Nature* **432**, 24.
- DANIEL, A.S., JOACHIM, L., FRIEDRICH, H., EDUARDAS, J., ELHAM, F. & YIANNOS, M. 2016 A parallel-SSHI rectifier for piezoelectric energy harvesting of periodic and shock excitations. *IEEE J. Solid-State Circuits* **51** (12), 2867–2879.
- DE MARQUI, C. JR., ERTURK, A. & INMAN, D.J. 2010 Piezoaeroelastic modeling and analysis of a generator wing with continuous and segmented electrodes. *J. Intell. Mater. Syst. Struct.* **21**, 983–993.
- DIAS, J., DE MARQUI, C. JR. & ERTURK, A. 2014 Three-degree-of-freedom hybrid piezoelectric-inductive aeroelastic energy harvester exploiting a control surface. *AIAA J.* **53**, 394–404.
- DOARÉ, O. & MICHELIN, S. 2011 Piezoelectric coupling in energy-harvesting fluttering flexible plates: linear stability analysis and conversion efficiency. *J. Fluids Struct.* **27**, 1357–1375.
- DU, X., WANG, Y., CHEN, H., LI, C., HAN, Y., YURCHENKO, D., WANG, J. & YU, H. 2022 Vortex-induced piezoelectric cantilever beam vibration for ocean wave energy harvesting via airflow from the orifice of oscillation water column chamber. *Nano Energy* **104**, 107870.
- DUNNMON, J.A., STANTON, S.C., MANN, B.P. & DOWELL, E.H. 2011 Power extraction from aeroelastic limit cycle oscillations. *J. Fluids Struct.* **27**, 1182–1198.
- GIACOMELLO, A. & PORFIRI, M. 2011 Underwater energy harvesting from a heavy flag hosting ionic polymer metal composites. *J. Appl. Phys.* **109**, 084903.
- GOLDSTEIN, D., HANDLER, R. & SIROVICH, L. 1993 Modelling a no-slip flow boundary with an external force field. *J. Comput. Phys.* **105**, 354–366.
- HAMLEHDAR, M., KASAEIAN, A. & SAFAEI, M.R. 2019 Energy harvesting from fluid flow using piezoelectrics: a critical review. *Renew. Energy* **143**, 1826–1838.
- HOBBS, W.B. & HU, D.L. 2012 Tree-inspired piezoelectric energy harvesting. *J. Fluids Struct.* **28**, 103–114.
- HUANG, W.X., SHIN, S.J. & SUNG, H.J. 2007 Simulation of flexible filaments in a uniform flow by the immersed boundary method. *J. Comput. Phys.* **226**, 2206–2228.
- HUANG, H., WEI, H. & LU, X.-Y. 2018 Coupling performance of tandem flexible inverted flags in a uniform flow. *J. Fluid Mech.* **837**, 461–476.
- JACKSON, J.D. 1998 *Classical Electrodynamics*, 3rd edn. Wiley.
- KANOUN, O. 2018 *Energy Harvesting for Wireless Sensor Networks: Technology, Components and System Design*. De Gruyter Oldenbourg.
- KIM, K., BAEK, S.J. & SUNG, H.J. 2002 An implicit velocity decoupling procedure for the incompressible Navier–Stokes equations. *Intl J. Numer. Meth. Fluids* **38**, 125–138.
- KIM, D., COSSE, J., CERDEIRA, C.H. & GHARIB, M. 2013 Flapping dynamics of an inverted flag. *J. Fluid Mech.* **736**, R1.
- KUTZ, J.N., BRUNTON, S.L., BRUNTON, B.W. & PROCTOR, J.L. 2016 *Dynamic Mode Decomposition: Data-Driven Modeling of Complex Systems*. SIAM-Society for Industrial and Applied Mathematics.
- LEFEUVRE, E., BADEL, A., RICHARD, C., PETIT, L. & GUYOMAR, D. 2006 A comparison between several vibration-powered piezoelectric generators for standalone systems. *Sensors Actuators A* **126** (2), 405–416.
- LI, S., ROY, A. & CALHOUN, B.H. 2019 A piezoelectric energy-harvesting system with parallel-SSHI rectifier and integrated maximum-power-point tracking. *IEEE Solid-State Circuits Lett.* **2** (12), 301–304.
- MAZHARMANESH, S., YOUNG, J., TIAN, F.-B., RAVI, S. & LAI, J.C.S. 2022 Energy harvesting of inverted piezoelectric flags in an oscillating flow. *J. Fluids Struct.* **115**, 103762.
- MICHELIN, S. & DOARÉ, O. 2013 Energy harvesting efficiency of piezoelectric flags in axial flows. *J. Fluid Mech.* **714**, 489–504.
- MITCHESON, P.D., YEATMAN, E.I.C. M., RAO, G.K., HOLMES, A.S. & GREEN, T.C. 2008 Energy harvesting from human and machine motion for wireless electronic devices. *Proc. IEEE* **96**, 1457–1486.
- PANDA, P.K. 2009 Environmental friendly lead-free piezoelectric materials. *J. Mater. Sci.* **44**, 5049–5062.
- PAULO, J.F.C. & GASPAS, P.D. 2010 Review and future trend of energy harvesting methods for portable medical devices. In *Proceedings of the World Congress on Engineering* (ed. S.I. Ao, L. Gelman, D.W.L. Hukins, A. Hunter & A.M. Korsunsky). Newswood Limited.
- PESKIN, C.S. 2002 The immersed boundary method. *Acta Numerica* **11**, 479–517.
- PETRINI, F. & GKOUKAS, K. 2018 Piezoelectric energy harvesting from vortex shedding and galloping induced vibrations inside HVAC ducts. *Energy Build.* **158**, 371–383.
- PIÑEIRUA, M., DOARÉ, O. & MICHELIN, S. 2015 Influence and optimization of the electrodes position in a piezoelectric energy harvesting flag. *J. Sound Vib.* **346**, 200–215.

- QADRI, M.N.M., ZHAO, F.W. & TANG, H. 2020 Fluid–structure interaction of a fully passive flapping foil for flow energy extraction. *Intl J. Mech. Sci.* **177**, 105587.
- RYU, J., PARK, S.G., KIM, B. & SUNG, H.J. 2015 Flapping dynamics of an inverted flag in a uniform flow. *J. Fluids Struct.* **57**, 159–169.
- SAFAEI, M., SODANO, H.A. & ANTON, S.R. 2019 A review of energy harvesting using piezoelectric materials: state-of-the-art a decade later (2008–2018). *Smart Mater. Struct.* **28**, 113001.
- SARKER, M.R., JULAI, S., SABRI, M.F.M., SAID, S.M., ISLAM, M.M. & TAHIR, M. 2019 Review of piezoelectric energy harvesting system and application of optimization techniques to enhance the performance of the harvesting system. *Sensors Actuators A* **300**, 111634.
- SHAIKH, F.K. & ZEADALLY, S. 2016 Energy harvesting in wireless sensor networks: a comprehensive review. *Renew. Sustain. Energy Rev.* **55**, 1041–1054.
- SHOELE, K. & MITTAL, R. 2016 Energy harvesting by flow-induced flutter in a simple model of an inverted piezoelectric flag. *J. Fluid Mech.* **790**, 582–606.
- SINGH, K., MICHELIN, S. & DE LANGRE, E. 2012 The effect of non-uniform damping on flutter in axial flow and energy-harvesting strategies. *Proc. R. Soc. A* **468**, 3620–3635.
- SODANO, H.A., INMAN, D.J. & PARK, G. 2004 A review of power harvesting from vibration using piezoelectric materials. *Shock Vib. Dig.* **36** (3), 197–206.
- SONG, R., SHAN, X., LV, F. & XIE, T. 2015 A study of vortex-induced energy harvesting from water using PZT piezoelectric cantilever with cylindrical extension. *Ceram. Intl* **41**, S768–S773.
- STOJCEV, M.K., KOSANOVIC, M.R. & GOLUBOVIC, L.R. 2009 Power management and energy harvesting techniques for wireless sensor nodes. In *2009 9th International Conference on Telecommunications in Modern Satellite, Cable and Broadcasting Services (IEEE)*.
- TAMIMI, V., WU, J., ESFEHANI, M.J., ZEINODDINI, M. & NAEENI, S.T.O. 2022 Comparison of hydrokinetic energy harvesting performance of a fluttering hydrofoil against other flow-induced vibration (FIV) mechanisms. *Renew. Energy* **186**, 157–172.
- TAN, T. & YAN, Z. 2017 Electromechanical decoupled model for cantilever-beam piezoelectric energy harvesters with inductive-resistive circuits and its application in galloping mode. *Smart Mater. Struct.* **26** (3), 035062.
- TAN, T., YAN, Z. & HAJJ, M. 2016 Electromechanical decoupled model for cantilever-beam piezoelectric energy harvesters. *Appl. Phys. Lett.* **109**, 101908.
- TAN, T., ZUO, L. & YAN, Z. 2021 Environment coupled piezoelectric galloping wind energy harvesting. *Sensors Actuators A* **323**, 112641.
- TANG, C., LIU, N.S. & LU, X.Y. 2015 Dynamics of an inverted flexible plate in a uniform flow. *Phys. Fluids* **27** (7), 073601.
- TAYLOR, G.W., BURNS, J.R., KAMMANN, S.A., POWERS, W.B. & WELSH, T.R. 2001 The energy harvesting eel: a small subsurface ocean/river power generator. *IEEE J. Ocean. Engng* **26**, 539–547.
- UCHINO, K. 2018 Piezoelectric energy harvesting systems—essentials to successful developments. *Energy Technol.* **6**, 829–848.
- WANG, X., ALBEN, S., LI, C. & YOUNG, Y.L. 2016 Stability and scalability of piezoelectric flags. *Phys. Fluids* **28**, 023601.
- WANG, Z., DU, L., ZHAO, J., THOMPSON, M.C. & SUN, X. 2020 Flow-induced vibrations of a pitching and plunging airfoil. *J. Fluid Mech.* **885**, A36.
- WANG, D.A. & KO, H.H. 2010 Piezoelectric energy harvesting from flow-induced vibration. *J. Micromech. Microengng* **20** (2), 025019.
- WANG, D.A. & LIU, N.Z. 2011 A shear mode piezoelectric energy harvester based on a pressurized water flow. *Sensors Actuators A* **167**, 449–458.
- XIA, Y., MICHELIN, S. & DOARÉ, O. 2015 Fluid-solid-electric lock-in of energy-harvesting piezoelectric flags. *Phys. Rev. Appl.* **3**, 014009.
- XU-XU, J., BARRERO-GIL, A. & VELAZQUEZ, A. 2016 Dual mass system for enhancing energy extraction from vortex-induced vibration of a circular cylinder. *Intl J. Mar. Energy* **16**, 250–261.
- ZHAO, F.W., QADRI, M.N.M., WANG, Z.K. & TANG, H. 2021 Flow-energy harvesting using a fully passive flapping foil: a guideline on design and operation. *Intl J. Mech. Sci.* **197**, 106323.
- ZHU, Q. 2011 Optimal frequency for flow energy harvesting of a flapping foil. *J. Fluid Mech.* **675**, 495–517.
- ZHU, Q. & PENG, Z. 2009 Mode coupling and flow energy harvesting by a flapping foil. *Phys. Fluids* **21**, 033601.